ELECTROMAGNETIC INDUCTION IN THE EARTH'S MANTLE AND OCEANS

Forward and inverse modelling

Jakub Velímský

Department of Geophysics
Faculty of Mathematics and Physics
Charles University

Habilitation thesis
Field: Geophysics
Prague 2019

Contents

1 Introduction **9**

2 Forward modelling **13**

2.1 The electromagnetic induction equation in a spherical Earth 13

2.2 Spherical harmonic approach 20

2.3 Assembly of the linear problem 22

2.4 Time discretization and linear problem solution 32

3 Inverse modelling **37**

3.1 Global EM induction inverse problem 37

3.2 Model parameters 38

3.3 External and internal sources 40

3.4 Data and misfit 41

3.5 Solution of the inverse problem 44

4 Conclusions **45**

4.1 Selected applications 45

4.2 Ongoing research and future outlook 47

A Appendices **59**

A.1 Electrical conductivity in the Earth's mantle inferred from CHAMP satellite measurements — I. Data processing and 1-D inversion 61

A.2 Electrical conductivity in the lower mantle: Constraints from CHAMP satellite data by time-domain EM induction modelling 63
A.3 Effect of a metallic core on transient geomagnetic induction 65
A.4 On the detectability of 3-D postperovskite distribution in D" by electromagnetic induction 67
A.5 Determination of three-dimensional distribution of electrical conductivity in the Earth's mantle from Swarm satellite data: Time-domain approach 69
A.6 Fast calculations of the gradient and the Hessian in the time-domain global electromagnetic induction inverse problem 71
A.7 On the modelling of M_2 tidal magnetic signatures: Effects of physical approximations and numerical resolution 73
A.8 The Global Toroidal Magnetic Field Generated in the Earth's Oceans . 75

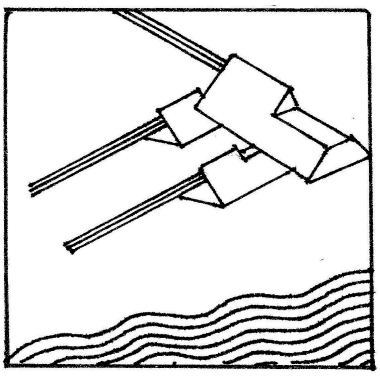

Preface

The subject of this Thesis is the problem of forward and inverse modelling of the physical phenomenon of electromagnetic induction on a global planetary scale and studies of the electric conductivity of the deep Earth. I was attracted to this topic during my doctoral studies at the Charles University, where I have developed the initial version of the forward solver based on the application of the spherical harmonic-finite element method in the time domain. My research in the last 20 years has been dedicated to this phenomenon, driven by the ever increasing capabilities of recent computers on the one side, and by the availability of low-orbit satellite measurements of the geomagnetic field on the other side.

My initial experience with interpretation of satellite geomagnetic data came from the German CHAMP (**CHA**llenging **M**inisatellite **P**ayload) mission (2000–2010). Since 2008 I have been involved in the preparation of the **Swarm** multi-satellite mission of the European Space Agency. During the development phase, the original time-domain three-dimensional (3-D) inversion method has been introduced. Following the Swarm launch in 2013, the first attempts to invert the satellite data in terms of 3-D mantle conductivity structure have pointed out that a proper separation of the external fields and their induced counterparts, a necessary step prior the solution of the inverse problem, represents a significant challenge. As of 2019, almost six years into the mission life, it seems that the 3-D inversion of satellite data is finally within sight.

As Swarm measurements have been accumulated and processing methods improved, I have turned my interest to the problem of motionally induced electric currents in the Earth's oceans, both by tidally and atmospherically driven ocean flows. While the magnetic signatures of the tidal flows have been successfully detected in the satellite data, the magnetic fields induced by the global ocean circulation, and thus closely related to the Earth's climate devel-

opment, still evade satellite detection.

During my research career, I had the opportunity to collaborate with many excellent colleagues at the Charles University, Prague, the Texas A&M University, College Station, the Eidgenössische Technische Hochschule, Zürich, within the Swarm DISC Consortium, and elsewhere. I would like to thank in particular Ondřej Čadek, Hana Čížková, David Einšpigel, Mark E. Everett, Chris Finlay, Alexander Grayver, Ladislav Hanyk, Andy Jackson, Alexey Kuvshinov, Zdeněk Martinec, Ctirad Matyska, Nils Olsen, Ondřej Souček, Libor Šachl, and Ľubica Valentová.

I would also like to acknowledge the support of the Grant Agency of the Czech Republic (Project No. P210/17-03689S), and the European Space Agency (Contracts No. 4000109562/14/NL/CBi and 4000109587/13/I-NB). In the last few years, I have exploited the computational resources of the *IT4Innovations National Supercomputing Center,* provided by The Ministry of Education, Youth and Sports from the Large Infrastructures for Research, Experimental Development and Innovations Project LM2015070.

Jakub Velímský

Prague, June 2019

1 Introduction

The electric conductivity is an important geophysical parameter connected to the thermal, chemical, and mineralogical state of the Earth's mantle. A traditional technique to study the distribution of electric conductivity in deep regions of the Earth is the electromagnetic induction (EMI) method. Two basic components are needed for the reconstruction of the conductivity model from observed variations of geomagnetic or geoelectric field. The *forward modelling* uniquely predicts, within the limits of the spatio-temporal resolution, the observable properties for a given conductivity model and a model of external or internal sources. This prediction is based on the numerical solution of the quasi-stationary Maxwell equations, or the electromagnetic induction equation derived directly from them. The *inverse modelling* then attempts to construct a conductivity model that explains the observed data within prescribed error limit. The solution of such a problem is inherently non-unique and additional constraints are applied to the conductivity model, based on some a-priori known geophysical informations, or as mathematical regularization of the models.

The EMI process on the global scale is driven by three main sources of energy. The charged particles trapped in the Earth's magnetosphere create a system of electric currents. The ring current consisting of mostly hydrogen ions circulating clockwise at distances of 3–8 Earth radii in the equatorial plane, is the most prominent energy source, capable of inducing electric currents even in the lower mantle. The main challenge in the area of global inversion of satellite data driven by the magnetospheric currents is the separation of the primary, inducing components, and the secondary, induced fields. These can be described by the time series of external and internal spherical harmonic coefficients. Such time series are one of the products of the Swarm mission. Since the rather critical assessment of the early versions of this product by Martinec et al. (2018), the situation has improved significantly, and a preliminary result of

the inversion of the most recent dataset will be presented at the end of this thesis.

The geomagnetic solar daily variations, the Sq signals, are used in electromagnetic induction studies to estimate the electric conductivity of the Earth's upper mantle. Traditionally, Sq induction studies employ the observatory magnetic data from a few quiet days, separate them into external (due to the ionospheric Sq current system) and internal (due to induced counterpart in the Earth) parts, and interpret the latter part in terms of the upper mantle electric conductivity. So far, global-scale 1-D conductivity models (e.g. Campbell and Anderssen, 1983; Campbell and Schiffmacher, 1988; Winch, 1984; Schmucker, 1999b) and regional 3-D models (e.g. Kuvshinov and Koch, 2015) have been determined from ground observatory data, the latter making use of a temporary station array.

A series of recent studies (Schnepf et al., 2015; Grayver et al., 2016, 2017; Velímský et al., 2018) has demonstrated the sensitivity of satellite-derived tidally-induced signals to mantle electric conductivity in the uppermost mantle. So far, only 1-D mantle profiles have been constrained with this approach, and a bias towards sub-oceanic mantle is obvious from the spatial distribution of the source signals.

The problem of forward EMI modelling on the global scale can be formulated either in the time domain, or in the frequency domain. The choice between the two approaches should be based on the characteristics of both sources and data. The daily geomagnetic variations in the ionosphere and the tidal signals in the oceans dominate at discrete frequencies related to the Earth rotation and orbital motions (Schmucker, 1999a; Einšpigel and Martinec, 2017). On the other hand, the time variations of the magnetospheric ring current are of transient nature (Martinec et al., 2018), and the large-scale atmospherically driven ocean circulation also covers physical phenomena with continuous spectrum in the range of days to years (Wunsch, 1981).

Various methods have been used to discretize and solve the forward problem with 3-D conductivity variations, as described in the comprehensive benchmark by Kelbert et al. (2014). The finite-difference methods (Uyeshima and Schultz, 2000; Kelbert et al., 2008, 2009) in the frequency domain typically apply staggered grids for the magnetic and electric fields. The computational domain involves the conductive Earth and the insulating atmosphere. The secondary field formulation can be exploited, as it allows the reduction of the computational

domain and increase of numerical solver accuracy. The finite-difference scheme yields a symmetric sparse system matrix with good numerical properties except in the vicinity of poles, where the grid singularities require special care. Local grid refinement is difficult to implement in the structured grids. A special class of unstructured finite differences was used by Weiss (2010).

The finite-element methods (Everett and Schultz, 1996; Yoshimura and Oshiman, 2002; Ribaudo et al., 2012; Grayver et al., 2019) can profit from the flexibility of the unstructured grids to describe complicated spatial geometries. The computational domain also comprises the insulating atmosphere. The system matrix is usually sparse and Hermitian, with a more complicated sparsity structure depending on the grid.

The contracting-integral-equation method (Pankratov et al., 1995; Singer, 1995; Kuvshinov, 2008) transforms the pre-Maxwell equations into a set of integral equations solved by Krylov-type iterative process. The Green functions are precalculated for a 1-D medium, and if chosen correctly, a fast iterative process with guranteed convergence can be achieved. The system matrix is dense, but its dimensions are limited to the area where lateral conductivity variations are present. However, the storage of the Green functions can have large memory requirements for calculations with high spatial resolution.

The spherical-harmonic approach has been presented for the first time by Martinec (1999) in the frequency domain, and later independently developed in the time domain by Hamano (2002) and Velímský and Martinec (2005). A detailed description of the recent developments, and discussion of its properties, is presented in this Thesis.

The methods of 3-D inverse modelling of global EMI have been so far exclusively based on the application of deterministic approaches to minimize a data misfit over a space of regularized conductivity models (Kelbert et al., 2008, 2009; Kuvshinov and Semenov, 2012; Semenov and Kuvshinov, 2012; Püthe and Kuvshinov, 2013; Velímský, 2013; Sun et al., 2015). The Bayesian approach as suggested by Pankratov and Kuvshinov (2016) is still computationally prohibitive due to the extreme number of forward calculations to be carried out to obtain sufficient sampling of probability density functions in large-dimensional spaces. However, the fast calculations of Hessians (Pankratov and Kuvshinov, 2015; Maksimov and Velímský, 2017) enable to perform a-posteriori error and sensitivity analysis even for the problems solved

by the deterministic approaches. A comprehensive overview of recent advances in the area of global EMI forward and inverse modelling is given by Kuvshinov (2015).

This thesis consists of two main parts. Chapters 2 and 3 are respectively dedicated to the recent developments of the forward and inverse EMI problems in spherical domain. The spherical harmonic-finite element approach implemented both in the time and frequency domains represents a flexible tool to deal with both external and interior sources. The question of scaling on shared- and distributed-memory parallel architectures is also discussed. The second part of the thesis introduces the applications of this methodology to selected problems.

2 Forward modelling

2.1 The electromagnetic induction equation in a spherical Earth

The electromagnetic fields inside the Earth or other solid celestial objects, and in their near-space environments, are governed by the conventional non-relativistic Maxwell equations,

$$\operatorname{curl} \boldsymbol{H} = \boldsymbol{j} + \frac{\partial \boldsymbol{D}}{\partial t}, \tag{2.1}$$

$$\operatorname{curl} \boldsymbol{E} = -\frac{\partial \boldsymbol{B}}{\partial t}, \tag{2.2}$$

$$\operatorname{div} \boldsymbol{B} = 0, \tag{2.3}$$

$$\operatorname{div} \boldsymbol{D} = \rho_{\mathrm{f}}, \tag{2.4}$$

where $\boldsymbol{H}(\boldsymbol{r};t)$, $\boldsymbol{B}(\boldsymbol{r};t)$, $\boldsymbol{E}(\boldsymbol{r};t)$, $\boldsymbol{D}(\boldsymbol{r};t)$, $\boldsymbol{j}(\boldsymbol{r};t)$, and $\rho_{\mathrm{f}}(\boldsymbol{r};t)$ denote respectively the magnetic field intensity, magnetic flux density, electric field, electric displacement, free current density, and the free charge density. As shown by Tyler and Mysak (1995), the equations (2.1–2.3) are valid for geophysical applications even in the coordinate frame anchored to a rotating planetary body. We will use the spherical coordinates $\boldsymbol{r} = (r, \vartheta, \varphi)$, where r, ϑ, and φ stand for radius, colatitude and longitude. We will represent the Earth by a spherical domain G with outer boundary ∂G at $r = a$, and the outer normal $\boldsymbol{e}_{\mathrm{r}}$.

The Earth materials are both electrically and magnetically linear, homogeneous, and isotropic, and thus described by the scalar constant electric permittivity ε, and magnetic permeability μ,

$$\boldsymbol{D} = \varepsilon \boldsymbol{E}, \tag{2.5}$$

$$\boldsymbol{B} = \mu \boldsymbol{H}. \tag{2.6}$$

In the area of global EMI, we are usually not interested in phenomena on the sub-second time scales. With relative permittivities of the Earth materials below 100, the displacement

currents can be neglected, and the Ampère law takes the pre-Maxwell form,

$$\operatorname{curl} \boldsymbol{H} = \boldsymbol{j}. \tag{2.7}$$

The magnetic permeability is assumed to take the value of the vacuum, $\mu = \mu_0$.

The Ohm's law, relating the electric current density to the electric field by a linear dependence, is usally assumed in the heterogeneous, isotropic form for a conductive continuum moving with velocity $\boldsymbol{v}(\boldsymbol{r}; t)$,

$$\boldsymbol{j} = \sigma \left(\boldsymbol{E} + \boldsymbol{v} \times \boldsymbol{B} \right). \tag{2.8}$$

The electric conductivity $\sigma(\boldsymbol{r}; t)$ can generally vary both in space and time. In the Earth's solid crust and mantle, the motional induction has negligible effect, and we can safely assume $\boldsymbol{v} = \boldsymbol{0}$. The time variations of the electric conductivity are also neglected there. As the distribution of electric conductivity is governed by the Earth's temperature and chemical and mineralogical composition, the radial dependence usually dominates the lateral variations. The important class of spherically symmetric (1-D) conductivity models $\sigma(r)$ has been traditionally employed both in forward and inverse modelling, either as a direct constraint, or as a tool to provide preconditioning and obtain faster convergence rates in full three-dimensional scenarios.

In the uppermost parts of the Earth, the lateral contrasts between the ionic conductivity of the salts dissolved in the seawater, and semi-conductive silicates are comparable to the radial variations. Moreover, the time variations of ocean conductivity should be taken into account due to the seasonal variations of temperature and salinity (Irrgang et al., 2016). As the Earth's main magnetic field $\boldsymbol{B}_{\mathrm{M}}(\boldsymbol{r}; t)$ dominates the induced fields by several orders of magnitude, the magnetic contribution to the Lorentz force in equation (2.8) usually takes the form

$$\boldsymbol{E}^{\mathrm{imp}} = \boldsymbol{v} \times \boldsymbol{B}_{\mathrm{M}}, \tag{2.9}$$

$$\boldsymbol{j}^{\mathrm{imp}} = \sigma \boldsymbol{E}^{\mathrm{imp}}, \tag{2.10}$$

$$\boldsymbol{j} = \sigma \left(\boldsymbol{E} + \boldsymbol{E}^{\mathrm{imp}} \right) = \sigma \boldsymbol{E} + \boldsymbol{j}^{\mathrm{imp}}, \tag{2.11}$$

where $\boldsymbol{E}^{\mathrm{imp}}(\boldsymbol{r}; t)$ and $\boldsymbol{j}^{\mathrm{imp}}(\boldsymbol{r}; t)$ denote the imposed electric field (the Lorentz force per unit charge), or corresponding imposed electric current, respectively.

Combining the equations (2.2) and (2.6–2.8) yields a single equation for the magnetic field vector, the EMI equation,

$$\mathrm{curl}\,\left(\frac{1}{\sigma}\mathrm{curl}\,\boldsymbol{B}\right)+\mu_0\frac{\partial\boldsymbol{B}}{\partial t}=\mu_0\mathrm{curl}\,\boldsymbol{E}^{\mathrm{imp}}. \tag{2.12}$$

Equivalently, the EMI equation can be transformed to the frequency domain, assuming time-invariant electric conductivity $\sigma(\boldsymbol{r})$, and harmonic-type dependence of the vectors

$$\boldsymbol{B}(\boldsymbol{r};t)=\mathrm{Re}\left\{\tilde{\boldsymbol{B}}\exp(-\mathrm{i}\omega\mu_0 t)\right\}, \tag{2.13}$$

$$\boldsymbol{E}^{\mathrm{imp}}(\boldsymbol{r};t)=\mathrm{Re}\left\{\tilde{\boldsymbol{E}}^{\mathrm{imp}}\exp(-\mathrm{i}\omega\mu_0 t)\right\}. \tag{2.14}$$

Then we can write

$$\mathrm{curl}\,\left(\frac{1}{\sigma}\mathrm{curl}\,\tilde{\boldsymbol{B}}\right)-\mathrm{i}\omega\mu_0\tilde{\boldsymbol{B}}=\mu_0\mathrm{curl}\,\tilde{\boldsymbol{E}}^{\mathrm{imp}}. \tag{2.15}$$

To complete the formulation, the initial and boundary conditions must be specified.

For the initial condition $\boldsymbol{B}(\boldsymbol{r};0)$ in the time-domain, it is sufficient to assume that

$$\mathrm{div}\,\boldsymbol{B}(\boldsymbol{r};0)=0. \tag{2.16}$$

Applying the div operator to the EMI equation (2.12) then assures that

$$\frac{\partial}{\partial t}\mathrm{div}\,\boldsymbol{B}(\boldsymbol{r};t)=0, \tag{2.17}$$

and hence the Gauss law (2.3) is satisfied for $t\geqslant 0$.

The choice of the boundary conditions applied at the Earth's surface $r=a$ is more complicated. The Earth's atmosphere is a very effective insulator, with electric conductivities ranging from 10^{-14} to $10^{-9}\,\mathrm{S/m}$ (Seran et al., 2017). Therefore, it can be approximated by a perfect insulator, where the magnetic field is fully described by a scalar magnetic potential $U(\boldsymbol{r};t)$, satisfying the Laplace equation,

$$\Delta U=0, \tag{2.18}$$

$$\boldsymbol{B}=-\mathrm{grad}\,U, \tag{2.19}$$

for $r\geqslant a$ and any $t\geqslant 0$.

The general boundary conditions stemming from the integral form of the Maxwell equations are

$$[\boldsymbol{e}_{\mathrm{r}} \times \boldsymbol{B}]^{+}_{-} = \mu_0 \boldsymbol{j}_{\mathrm{S}} \qquad \text{at } \partial G, \tag{2.20}$$

$$[\boldsymbol{e}_{\mathrm{r}} \cdot \boldsymbol{B}]^{+}_{-} = 0 \qquad \text{at } \partial G, \tag{2.21}$$

$$[\boldsymbol{e}_{\mathrm{r}} \times \boldsymbol{E}]^{+}_{-} = \boldsymbol{0} \qquad \text{at } \partial G, \tag{2.22}$$

where $[\circ]^{+}_{-}$ denotes the discontinuity across the interface, and $\boldsymbol{j}_{\mathrm{S}}(\boldsymbol{r}; t)$ is the surface current density. Here we assume that $\boldsymbol{j}_{\mathrm{S}} = \boldsymbol{0}$. However, note that the thin-sheet currents can be effectively employed in a two-dimensional formulation in some specific applications involving induction in the oceans (Kuvshinov et al., 2007; Sun and Egbert, 2012, among many others).

In order to proceed with the application of the boundary conditions, we need to apply the Helmholtz decomposition, including the toroidal-poloidal splitting, to both the magnetic and electric fields. An arbitrary vector field $\boldsymbol{f}(\boldsymbol{r})$, sufficiently smooth, and decaying in the case of unbounded domain, can be decomposed into the irrotational (scaloidal) and divergence-free (solenoidal) components, the latter consisting of the toroidal and poloidal parts, (Arfken and Weber, 2005; Backus, 1986),

$$\boldsymbol{f}(\boldsymbol{r}) = \boldsymbol{f}_{\mathrm{S}}(\boldsymbol{r}) + \boldsymbol{f}_{\mathrm{T}}(\boldsymbol{r}) + \boldsymbol{f}_{\mathrm{P}}(\boldsymbol{r}), \tag{2.23}$$

$$\boldsymbol{f}_{\mathrm{S}}(\boldsymbol{r}) = \operatorname{grad} \Xi(\boldsymbol{r}), \tag{2.24}$$

$$\boldsymbol{f}_{\mathrm{T}}(\boldsymbol{r}) = \operatorname{curl} \left[\boldsymbol{r}\Psi(\boldsymbol{r})\right], \tag{2.25}$$

$$\boldsymbol{f}_{\mathrm{P}}(\boldsymbol{r}) = \operatorname{curl}\operatorname{curl} \left[\boldsymbol{r}\Phi(\boldsymbol{r})\right]. \tag{2.26}$$

The individual components are described by respective scalar functions $\Xi(\boldsymbol{r})$, $\Psi(\boldsymbol{r})$, and $\Phi(\boldsymbol{r})$,

and satisfy the following properties,

$$\operatorname{curl} \boldsymbol{f}_{\mathrm{S}} = \mathbf{0}, \tag{2.27}$$

$$\operatorname{div} \boldsymbol{f}_{\mathrm{T}} = 0, \tag{2.28}$$

$$\operatorname{div} \boldsymbol{f}_{\mathrm{P}} = 0, \tag{2.29}$$

$$\boldsymbol{e}_{\mathrm{r}} \cdot \boldsymbol{f}_{\mathrm{T}} = 0, \tag{2.30}$$

$$\boldsymbol{e}_{\mathrm{r}} \cdot \operatorname{curl} \boldsymbol{f}_{\mathrm{P}} = 0, \tag{2.31}$$

$$\operatorname{div}_{\mathrm{H}} \boldsymbol{f}_{\mathrm{T}} = 0, \tag{2.32}$$

$$\boldsymbol{f}_{\mathrm{S}} = \boldsymbol{e}_{\mathrm{r}} \frac{\partial \Xi}{\partial r} + \operatorname{grad}_{\mathrm{H}} \Xi, \tag{2.33}$$

$$\boldsymbol{f}_{\mathrm{P}} = -\boldsymbol{r} \Delta_{\mathrm{H}} \Phi + \operatorname{grad}_{\mathrm{H}} \left(r \frac{\partial \Phi}{\partial r} + \Phi \right). \tag{2.34}$$

In the last formulas, we have separated the radial and lateral parts of the scaloidal and poloidal fields by splitting the gradient and Laplacian operators,

$$\operatorname{grad} = \boldsymbol{e}_{\mathrm{r}} \frac{\partial}{\partial r} + \operatorname{grad}_{\mathrm{H}} = \boldsymbol{e}_{\mathrm{r}} \frac{\partial}{\partial r} + \frac{1}{r} \operatorname{grad}_{\Omega}, \tag{2.35}$$

$$\Delta = \frac{\partial^2}{\partial r^2} + \frac{2}{r} \frac{\partial}{\partial r} + \Delta_H. \tag{2.36}$$

Note also, that both the curl and $\boldsymbol{e}_{\mathrm{r}}\times$ operators convert a toroidal field into poloidal and vice versa. Now we can demonstrate that an arbitrary toroidal field is orthogonal to any poloidal or scaloidal components on an arbitrary spherical surface, such as ∂G,

$$\begin{aligned} \int_{\partial G} \boldsymbol{f}_{\mathrm{T}} \cdot \boldsymbol{f}_{\mathrm{P}} \mathrm{d}S &= \int_{\partial G} \boldsymbol{f}_{\mathrm{T}} \cdot \operatorname{grad}_{\mathrm{H}} \left(r \frac{\partial \Phi}{\partial r} + \Phi \right) \mathrm{d}S = \\ &= \int_{\partial G} \operatorname{div}_{\mathrm{H}} \left[\boldsymbol{f}_{\mathrm{T}} \left(r \frac{\partial \Phi}{\partial r} + \Phi \right) \right] \mathrm{d}S = 0, \end{aligned} \tag{2.37}$$

$$\begin{aligned} \int_{\partial G} \boldsymbol{f}_{\mathrm{T}} \cdot \boldsymbol{f}_{\mathrm{S}} \mathrm{d}S &= \int_{\partial G} \boldsymbol{f}_{\mathrm{T}} \cdot \operatorname{grad}_{\mathrm{H}} \Xi \mathrm{d}S = \\ &= \int_{\partial G} \operatorname{div}_{\mathrm{H}} \left(\boldsymbol{f}_{\mathrm{T}} \Xi \right) \mathrm{d}S = 0. \end{aligned} \tag{2.38}$$

The last step follows from the application of the two-dimensional Gauss theorem on a closed surface ∂G (Berger and Hornig, 2018).

Since the toroidal field is zero in the insulator (Backus, 1986), the boundary conditions (2.20–2.21) can be written as

$$\boldsymbol{e}_{\mathrm{r}} \times \boldsymbol{B}_{\mathrm{T}} = \boldsymbol{0} \qquad \text{at } \partial G, \tag{2.39}$$

$$\boldsymbol{e}_{\mathrm{r}} \times \boldsymbol{B}_{\mathrm{P}} = -\boldsymbol{e}_{\mathrm{r}} \times \operatorname{grad} U \qquad \text{at } \partial G, \tag{2.40}$$

$$\boldsymbol{e}_{\mathrm{r}} \cdot \boldsymbol{B}_{\mathrm{P}} = -\boldsymbol{e}_{\mathrm{r}} \cdot \operatorname{grad} U \qquad \text{at } \partial G. \tag{2.41}$$

Let us discuss the configuration of the boundary conditions necessary to obtain a unique solution of the time-domain EMI equation (2.12). Note that analogous derivations can be also carried out in the frequency domain. We will assume that two smooth solutions, $\boldsymbol{B}_1(\boldsymbol{r};t)$ and $\boldsymbol{B}_2(\boldsymbol{r};t)$, exist for the same internal forcing $\boldsymbol{E}^{\mathrm{imp}}(\boldsymbol{r};t)$, and both satisfy the same divergence-free initial condition $\boldsymbol{B}(\boldsymbol{r};0)$. Then the difference $\delta\boldsymbol{B}(\boldsymbol{r};t) = \boldsymbol{B}_2(\boldsymbol{r};t) - \boldsymbol{B}_1(\boldsymbol{r};t)$ satisfies the homogeneous EMI equation

$$\operatorname{curl}\left(\frac{1}{\sigma}\operatorname{curl}\delta\boldsymbol{B}\right) + \mu_0\frac{\partial\delta\boldsymbol{B}}{\partial t} = \boldsymbol{0}. \tag{2.42}$$

Now we respectively multiply equation (2.42) by $\delta\boldsymbol{B}$ and integrate over G, apply the Green's curl-identity, and integrate over time from 0 to t,

$$\begin{aligned}
&\int_G \mu_0\delta\boldsymbol{B}\cdot\frac{\partial\delta\boldsymbol{B}}{\partial t}\mathrm{d}V + \int_G \delta\boldsymbol{B}\cdot\operatorname{curl}\left(\frac{1}{\sigma}\operatorname{curl}\delta\boldsymbol{B}\right)\mathrm{d}V = 0,\\
&\qquad\frac{\mu_0}{2}\frac{\partial}{\partial t}\int_G \delta\boldsymbol{B}^2\mathrm{d}V + \int_G \frac{1}{\sigma}\left(\operatorname{curl}\delta\boldsymbol{B}\right)^2\mathrm{d}V = \int_{\partial G}\frac{1}{\sigma}\left(\boldsymbol{e}_{\mathrm{r}}\times\delta\boldsymbol{B}\right)\cdot\operatorname{curl}\delta\boldsymbol{B}\mathrm{d}S,\\
&\frac{\mu_0}{2}\int_G \delta\boldsymbol{B}(t)^2\mathrm{d}V + \int_0^t\int_G \frac{\left(\operatorname{curl}\delta\boldsymbol{B}(\tau)\right)^2}{\sigma(\tau)}\mathrm{d}V\mathrm{d}\tau = \int_0^t\int_{\partial G}\left(\boldsymbol{e}_{\mathrm{r}}\times\delta\boldsymbol{B}(\tau)\right)\cdot\frac{\operatorname{curl}\delta\boldsymbol{B}(\tau)}{\sigma(\tau)}\mathrm{d}S\mathrm{d}\tau.
\end{aligned} \tag{2.43}$$

The integrands on the left-hand side of the last expression are non-negative. Therefore, any combination of boundary conditions that yields zero integral on the right-hand side of equation (2.43) will enforce $\delta\boldsymbol{B} = \boldsymbol{0}$ at all positions and times, and thus guarantee the uniqueness of the solution.

Using respectively the toroidal-poloidal and the scaloidal-toroidal-poloidal decomposition of the magnetic and electric field, the surface integral on the right-hand side of equation (2.43)

can be written with the help of the Ampère law (2.7), the orthogonality relations (2.37–2.38), and the poloidal-toroidal conversion property of the $\boldsymbol{e}_{\mathrm{r}}\times$ operator as

$$\int_0^t\!\!\int_{\partial G} (\boldsymbol{e}_{\mathrm{r}} \times \delta\boldsymbol{B}) \cdot \frac{\operatorname{curl}\delta\boldsymbol{B}}{\sigma}\mathrm{d}S\mathrm{d}\tau =$$

$$\mu_0 \int_0^t\!\!\int_{\partial G} (\boldsymbol{e}_{\mathrm{r}} \times \delta\boldsymbol{B}) \cdot \delta\boldsymbol{E}\,\mathrm{d}S\mathrm{d}\tau =$$

$$\mu_0 \int_0^t\!\!\int_{\partial G} \left[(\boldsymbol{e}_{\mathrm{r}} \times \delta\boldsymbol{B}_{\mathrm{T}}) \cdot (\delta\boldsymbol{E}_{\mathrm{S}} + \delta\boldsymbol{E}_{\mathrm{P}}) + (\boldsymbol{e}_{\mathrm{r}} \times \delta\boldsymbol{B}_{\mathrm{P}}) \cdot \delta\boldsymbol{E}_{\mathrm{T}}\right] \mathrm{d}S\mathrm{d}\tau, \tag{2.44}$$

where $\delta\boldsymbol{E}$ stands for the difference of electric fields corresponding to solutions $\boldsymbol{B}_1$ and $\boldsymbol{B}_2$.

Now we immediately see, that if both solutions $\boldsymbol{B}_1$ and $\boldsymbol{B}_2$ satisfy the boundary conditions (2.39) and (2.40), the difference $\delta\boldsymbol{B}$ satisfies their homogeneous form, zeroing out the surface integral (2.44), and via equation (2.43) implying that $\boldsymbol{B}_1(\boldsymbol{r};t) = \boldsymbol{B}_2(\boldsymbol{r};t)$ for any $\boldsymbol{r}$ and t. The vertical magnetic field at the surface is predicted by the EMI equation, and the boundary condition (2.41) applies to the scalar potential solution of the Laplace equation (2.18) in the atmosphere. The combination of boundary conditions (2.39) and (2.40) is the **Dirichlet** boundary condition.

What about other combinations of boundary conditions that will guarantee a unique solution? If we combine the zero surface toroidal magnetic field constraint (2.39) with prescribed toroidal electric field, i.e., $\delta\boldsymbol{E}_{\mathrm{T}} = \boldsymbol{0}$, the integral (2.44) is zero again, and the uniqueness of the EMI equation solution is guaranteed. Since

$$\boldsymbol{E}_{\mathrm{T}} = \left(\frac{\operatorname{curl}\boldsymbol{B}}{\mu_0\sigma}\right)_{\mathrm{T}}, \tag{2.45}$$

this is the case of **mixed** boundary condition. A Neumann-type condition is applied to the poloidal magnetic field solution, while a homogeneous Dirichlet-type condition (2.39) is still applied to the toroidal magnetic field. Note that the radial component of the Faraday law (2.2) reads as

$$\boldsymbol{e}_{\mathrm{r}} \cdot \operatorname{curl}\boldsymbol{E}_{\mathrm{T}} = -\boldsymbol{e}_{\mathrm{r}} \cdot \frac{\partial\boldsymbol{B}_{\mathrm{P}}}{\partial t}, \tag{2.46}$$

implying for the toroidal electric scalar function

$$\Delta_{\mathrm{H}}\Psi_E = \frac{1}{a}\boldsymbol{e}_{\mathrm{r}} \cdot \frac{\partial\boldsymbol{B}_{\mathrm{P}}}{\partial t}. \tag{2.47}$$

Thus, Ψ_E, and consequently $\boldsymbol{E}_{\mathrm{T}}$ can be obtained on ∂G from the time-derivative of the radial magnetic field (2.41). The horizontal poloidal magnetic field (2.40) is predicted by the EMI equation.

Another type of boundary condition, called **external**, is based on the separation of the potential field in the insulating atmosphere into the external part, with sources in the ionosphere and magnetosphere, and the internal part, corresponding to the magnetic fields induced in the Earth. The external component is prescribed, the internal component is predicted by the EMI equation. The toroidal magnetic field is still zero on the surface. In order to demonstrate that this approach also guarantees a unique solution, we have to introduce the spherical harmonic apparatus first.

2.2 Spherical harmonic approach

The spherical harmonic functions represent a powerful tool to parameterize the solutions of partial differential equations in spherical coordinates. Following Varshalovich et al. (1989), we define the fully normalized, complex, scalar spherical harmonic functions of degree j and order m, $|m| \leqslant j$, as

$$\tilde{Y}_{jm}(\Omega) = \sqrt{\frac{2j+1}{4\pi}\frac{(j-m)!}{(j+m)!}} P_j^m(\cos\vartheta)\, e^{\mathrm{i}m\varphi}, \tag{2.48}$$

where $P_j^m(\cos\vartheta)$ are the associated Legendre polynomials,

$$P_j^m(\cos\vartheta) = (-\sin\vartheta)^m \frac{\mathrm{d}^m}{(\mathrm{d}\cos\vartheta)^m} P_j(\cos\vartheta). \tag{2.49}$$

This basis is practical for the frequency-domain formulation of the EMI equation (2.15). In the case of time-domain formulation (2.12), only real-valued fields are used, and therefore, a real basis is preferred,

$$Y_{jm}(\Omega) = \begin{cases} \sqrt{2}\,(-1)^m \mathrm{Re}\tilde{Y}_{jm}(\Omega) & m > 0, \\ \tilde{Y}_{jm}(\Omega) & m = 0, \\ \sqrt{2}\,(-1)^m \mathrm{Im}\tilde{Y}_{j|m|}(\Omega) & m < 0, \end{cases} \tag{2.50}$$

where the sine-type harmonics are assigned to negative degrees and the cosine-type harmonics correspond to positive degrees. Both the complex- and real-valued spherical harmonics form

respectively the complete orthonormal bases of complex and real scalar functions on the surface of a unit sphere. The extension to vector functions is possible in several different ways. One possible approach is the use of the radial unit vector $\boldsymbol{e}_\mathrm{r}$ and the angular gradient operator grad_Ω to separate respectively the vertical poloidal-scaloidal, the toroidal, and the horizontal poloidal-scaloidal components of vector field, namely,

$$\boldsymbol{S}_{jm}^{(-1)}(\Omega) = Y_{jm}(\Omega)\boldsymbol{e}_\mathrm{r}, \tag{2.51}$$

$$\boldsymbol{S}_{jm}^{(0)}(\Omega) = \boldsymbol{e}_\mathrm{r} \times \mathrm{grad}_\Omega\, Y_{jm}(\Omega), \tag{2.52}$$

$$\boldsymbol{S}_{jm}^{(+1)}(\Omega) = \mathrm{grad}_\Omega\, Y_{jm}(\Omega). \tag{2.53}$$

The real-valued definition can be easily extended to complex vectors by replacing $Y_{jm}(\Omega)$ with $\tilde{Y}_{jm}(\Omega)$. The vector spherical harmonic functions are orthogonal on a unit sphere, with the norm

$$N_{j\lambda} = \delta_{\lambda,-1} + j(j+1)(\delta_{\lambda,0} + \delta_{\lambda,+1}), \tag{2.54}$$

and satisfy useful differential identities summarized for example in Maksimov and Velímský (2017, Appendix A).

The principal advantage of spherical harmonic formulation is the existence of an analytical solution of the Laplace equation for a scalar magnetic potential in the atmosphere (2.18) in the form of the infinite series,

$$U(\boldsymbol{r};t) = a\sum_{j=1}^{\infty}\sum_{m=-j}^{j}\left[G_{jm}^{(\mathrm{e})}(t)\left(\frac{r}{a}\right)^j + G_{jm}^{(\mathrm{i})}(t)\left(\frac{a}{r}\right)^{j+1}\right]Y_{jm}(\Omega), \tag{2.55}$$

for $r \geqslant a$. The coefficients $G_{jm}^{(\mathrm{e})}(t)$ and $G_{jm}^{(\mathrm{i})}(t)$ describe respectively the external and internal field with respect to the radius a. By expressing the magnetic field $\boldsymbol{B}(\boldsymbol{r};t)$ in the vector spherical harmonic basis

$$\boldsymbol{B}(\boldsymbol{r};t) = \sum_{j=1}^{\infty}\sum_{m=-j}^{j}\sum_{\lambda=-1}^{1} B_{jm}^{(\lambda)}(r;t)\boldsymbol{S}_{jm}^{(\lambda)}(\Omega), \tag{2.56}$$

for $r \leqslant a$, the boundary conditions (2.39–2.41) can be written as

$$B_{jm}^{(0)}(a;t) = 0, \tag{2.57}$$

$$B_{jm}^{(+1)}(a;t) = -\left[G_{jm}^{(\mathrm{e})}(t) + G_{jm}^{(\mathrm{i})}(t)\right], \tag{2.58}$$

$$B_{jm}^{(-1)}(a;t) = -\left[j\,G_{jm}^{(\mathrm{e})}(t) - (j+1)G_{jm}^{(\mathrm{i})}(t)\right]. \tag{2.59}$$

Let us now demonstrate the uniqueness of the EMI equation solution under the external field boundary condition, obtained by eliminating $G^{(\mathrm{i})}_{jm}(t)$ from equations (2.58–2.59),

$$B^{(0)}_{jm}(a;t) = 0, \tag{2.60}$$

$$B^{(-1)}_{jm}(a;t) + (j+1)B^{(+1)}_{jm}(a;t) = -(2j+1)G^{(\mathrm{e})}_{jm}(t). \tag{2.61}$$

By prescribing the zero toroidal field, and the same set of external field coefficients $G^{(\mathrm{e})}_{jm}(t)$ for the solutions $\boldsymbol{B}_1$ and $\boldsymbol{B}_2$, we can substitute $\delta B^{(0)}_{jm}(a;t) = 0$ and $\delta G^{(\mathrm{e})}_{jm}(t) = 0$ into the surface integral on the right-hand side of the equation (2.43). Taking into account the spherical harmonic representation of equation (2.46),

$$-\frac{j(j+1)}{a}\delta E^{(0)}_{jm}(a;t) = -\frac{\partial}{\partial t}\delta B^{(-1)}_{jm}(a;t), \tag{2.62}$$

we can therefore write

$$\begin{aligned}
\int_0^t\!\!\int_{\partial G} (\boldsymbol{e}_{\mathrm{r}} \times \delta\boldsymbol{B}) \cdot \delta\boldsymbol{E}\,\mathrm{d}S\mathrm{d}\tau &= \mu_0 a^2 \sum_{jm} j(j+1) \int_0^t \left[\delta B^{(+1)}_{jm}\delta E^{(0)}_{jm} - \delta B^{(0)}_{jm}\delta E^{(+1)}_{jm}\right]\mathrm{d}\tau \\
&= \mu_0 a^3 \sum_{jm} \int_0^t \left[\left(\delta G^{(\mathrm{e})}_{jm} + \delta G^{(\mathrm{i})}_{jm}\right)\frac{\partial}{\partial t}\left(j\delta G^{(\mathrm{e})}_{jm} - (j+1)\delta G^{(\mathrm{i})}_{jm}\right)\right]\mathrm{d}\tau \\
&= -\frac{\mu_0 a^3}{2}\sum_{jm}(j+1)\int_0^t \frac{\partial}{\partial t}\left(\delta G^{(\mathrm{i})}_{jm}\right)^2 \mathrm{d}\tau \\
&= -\frac{\mu_0 a^3}{2}\sum_{jm}(j+1)\left(\delta G^{(\mathrm{i})}_{jm}(t)\right)^2 \leqslant 0.
\end{aligned} \tag{2.63}$$

Setting $\delta G^{(\mathrm{i})}_{jm}(t) = 0\ \forall j < \infty, |m| \leqslant j$ is the only way to make the result compatible with the non-negative left-hand side of the equation (2.43), and hence $\delta\boldsymbol{B}(r;t) = \boldsymbol{0}$ everywhere and everytime. An analogous derivation can be carried out in the frequency domain.

2.3 Assembly of the linear problem

A straightforward approach to transform the time-domain or the frequency-domain EMI equation (2.12, 2.15) into a linear algebraic problem is the use of the Galerkin method. Firstly, the integral formulations of the problems are introduced, following Křížek and Neittaanmäki

(1996). Note that the integral formulation is used only for the spatial coordinates in the case of time-domain problems. The differential formulation in the time variable imposes more strict regularity requirements on the solution than the integral formulation. Using the definitions of functional spaces from Table 2.1, we can write for the cases of the Dirichlet, mixed, and the external boundary condition, respectively:

Time-domain EMI with the Dirichlet boundary condition

Let $\mu_0 > 0$ be the magnetic permeability, $\rho(r,\vartheta,\varphi;t) \in C^0\left(\overline{I};L^+_\infty(G,\mathbb{R})\right)$ the electric resistivity, and $\boldsymbol{E}^{\mathrm{imp}}(r,\vartheta,\varphi;t) \in C^0\left(\overline{I};L_2(G,\mathbb{R}^3)\right)$ the imposed electric field. Let $\boldsymbol{B}_0(\boldsymbol{r}) \in V_{0T}$ be the initial condition at $t_0 = 0$, and $\boldsymbol{B}^0(\boldsymbol{r};t) \in C^1\left(\overline{I};V_{0T}\right)$ the Dirichlet boundary condition $\boldsymbol{e}_{\mathrm{r}} \times \boldsymbol{B}^0(a,\vartheta,\varphi;t)$ extended from $r = a$ to the entire domain G. Find $\boldsymbol{B}(\boldsymbol{r};t) \in C^1\left(\overline{I};V_{0T}\right)$ such that $\boldsymbol{B} - \boldsymbol{B}^0 \in C^1\left(\overline{I};V_0\right)$, $\boldsymbol{B}(\boldsymbol{r};0) = \boldsymbol{B}_0(\boldsymbol{r})$, and

$$\int_G \left(\mu_0\,\delta\boldsymbol{B}\cdot\frac{\partial\boldsymbol{B}}{\partial t} + \rho\,\mathrm{curl}\,\delta\boldsymbol{B}\cdot\mathrm{curl}\,\boldsymbol{B}\right)\mathrm{d}V = \int_G \mu_0\,\mathrm{curl}\,\delta\boldsymbol{B}\cdot\boldsymbol{E}^{\mathrm{imp}}\mathrm{d}V, \tag{2.64}$$

$\forall\,\delta\boldsymbol{B}(\boldsymbol{r}) \in V_0$ and $\forall t \in I$.

Time-domain EMI with mixed boundary condition

Let $\mu_0 > 0$ be the magnetic permeability, $\rho(r,\vartheta,\varphi;t) \in C^0\left(\overline{I};L^+_\infty(G,\mathbb{R})\right)$ the electric resistivity, and $\boldsymbol{E}^{\mathrm{imp}}(r,\vartheta,\varphi;t) \in C^0\left(\overline{I};L_2(G,\mathbb{R}^3)\right)$ the imposed electric field. Let $\boldsymbol{B}_0(\boldsymbol{r}) \in V_{0T}$ be the initial condition at $t_0 = 0$, and $\boldsymbol{E}^0_T(\vartheta,\varphi;t) \in C^0\left(\overline{I};H^{\frac{1}{2}}(\partial G;\mathbb{R}^3)\right)$ the toroidal electric field at the surface, including the contribution from $-\boldsymbol{E}^{\mathrm{imp}}$. Find $\boldsymbol{B}(\boldsymbol{r};t) \in C^1\left(\overline{I};V_{0T}\right)$ such that $\boldsymbol{B}(\boldsymbol{r};0) = \boldsymbol{B}_0(\boldsymbol{r})$, and

$$\int_G \left(\mu_0\,\delta\boldsymbol{B}\cdot\frac{\partial\boldsymbol{B}}{\partial t} + \rho\,\mathrm{curl}\,\delta\boldsymbol{B}\cdot\mathrm{curl}\,\boldsymbol{B}\right)\mathrm{d}V = \int_G \mu_0\,\mathrm{curl}\,\delta\boldsymbol{B}\cdot\boldsymbol{E}^{\mathrm{imp}}\mathrm{d}V + \int_{\partial G}\mu_0\,(\boldsymbol{e}_{\mathrm{r}}\times\delta\boldsymbol{B})\cdot\boldsymbol{E}^0_T\,\mathrm{d}S, \tag{2.65}$$

$\forall\,\delta\boldsymbol{B}(\boldsymbol{r}) \in V_{0T}$ and $\forall t \in I$.

Time-domain EMI with external boundary condition

Let $\mu_0 > 0$ be the magnetic permeability, $\rho(r,\vartheta,\varphi;t) \in C^0\left(\overline{I};L^+_\infty(G,\mathbb{R})\right)$ the electric resistivity, and $\boldsymbol{E}^{\mathrm{imp}}(r,\vartheta,\varphi;t) \in C^0\left(\overline{I};L_2(G,\mathbb{R}^3)\right)$ the imposed electric field. Let $\boldsymbol{B}_0(\boldsymbol{r}) \in V_{0T}$ be the initial condition, at $t_0 = 0$, and $G^{(\mathrm{e})}_{jm}(t) \in C^1\left(\overline{I};\mathbb{R}\right)$ a set of external field coefficients for $j = 1,2,\ldots,\infty$ and $m = -j,\ldots,0,\ldots,+j$. Find $\boldsymbol{B}(\boldsymbol{r};t) \in C^1\left(\overline{I};V_{0T}\right)$ such that

$$\int_G \left(\mu_0\,\delta\boldsymbol{B}\cdot\frac{\partial\boldsymbol{B}}{\partial t} + \rho\,\mathrm{curl}\,\delta\boldsymbol{B}\cdot\mathrm{curl}\,\boldsymbol{B}\right)\mathrm{d}V = \int_G \mu_0\,\mathrm{curl}\,\delta\boldsymbol{B}\cdot\boldsymbol{E}^{\mathrm{imp}}\mathrm{d}V, \tag{2.66}$$

$\forall\,\delta\boldsymbol{B}(\boldsymbol{r}) \in V_0$ and $\forall t \in I$, and

$$\int_{\partial G}\left[\frac{1}{j}\boldsymbol{S}^{(+1)}_{jm} + \boldsymbol{S}^{(-1)}_{jm}\right]\cdot\boldsymbol{B}(\boldsymbol{r};t)\,\mathrm{d}S = -(2j+1)a^2G^{(\mathrm{e})}_{jm}(t), \tag{2.67}$$

$\forall\, j = 1,2,\ldots,\infty$ and $m = -j,\ldots,0,\ldots,+j$ and $\forall t \in I$.

Frequency-domain EMI with the Dirichlet boundary condition

Let $\omega > 0$ be the angular frequency, $\mu_0 > 0$ the magnetic permeability, $\rho(r,\vartheta,\varphi) \in L^+_\infty(G,\mathbb{R})$ the electric resistivity, and $\tilde{\boldsymbol{E}}^{\mathrm{imp}}(r,\vartheta,\varphi) \in L_2(G,\mathbb{C}^3)$ the imposed electric field. Let $\tilde{\boldsymbol{B}}^0(\boldsymbol{r}) \in \tilde{V}_{0T}$ be the Dirichlet boundary condition $\boldsymbol{e}_{\mathrm{r}} \times \tilde{\boldsymbol{B}}^0(a,\vartheta,\varphi)$ extended from $r = a$ to the entire domain G. Find $\tilde{\boldsymbol{B}}(\boldsymbol{r}) \in \tilde{V}_{0T}$ such that $\tilde{\boldsymbol{B}} - \tilde{\boldsymbol{B}}^0 \in \tilde{V}_0$, and

$$\int_G \left(-\mathrm{i}\omega\mu_0\,\delta\tilde{\boldsymbol{B}}^*\cdot\boldsymbol{B} + \rho\,\mathrm{curl}\,\delta\tilde{\boldsymbol{B}}^*\cdot\mathrm{curl}\,\boldsymbol{B}\right)\mathrm{d}V = \int_G \mu_0\,\mathrm{curl}\,\delta\tilde{\boldsymbol{B}}^*\cdot\tilde{\boldsymbol{E}}^{\mathrm{imp}}\mathrm{d}V, \tag{2.68}$$

$\forall\,\delta\tilde{\boldsymbol{B}}(\boldsymbol{r}) \in \tilde{V}_0$.

Frequency-domain EMI with mixed boundary condition

Let $\omega > 0$ be the angular frequency, $\mu_0 > 0$ the magnetic permeability, $\rho(r,\vartheta,\varphi) \in L^+_\infty(G,\mathbb{R})$ the electric resistivity, and $\tilde{\boldsymbol{E}}^{\mathrm{imp}}(r,\vartheta,\varphi) \in L_2(G,\mathbb{C}^3)$ the imposed electric field.

Let $\tilde{\boldsymbol{E}}_T^0(\vartheta,\varphi;t) \in \tilde{H}^{\frac{1}{2}}(\partial G;\mathbb{C}^3)$ be the toroidal electric field at the surface, including the contribution from $-\boldsymbol{E}^{\mathrm{imp}}$. Find $\tilde{\boldsymbol{B}}(\boldsymbol{r}) \in \tilde{V}_{0T}$ such that

$$\int_G \left(-\mathrm{i}\omega\mu_0\,\delta\tilde{\boldsymbol{B}}^*\cdot\boldsymbol{B} + \rho\,\mathrm{curl}\,\delta\tilde{\boldsymbol{B}}^*\cdot\mathrm{curl}\,\boldsymbol{B}\right)\mathrm{d}V = \tag{2.69}$$

$$\int_G \mu_0\,\mathrm{curl}\,\delta\tilde{\boldsymbol{B}}^*\cdot\tilde{\boldsymbol{E}}^{\mathrm{imp}}\mathrm{d}V + \int_{\partial G}\mu_0\left(\boldsymbol{e}_{\mathrm{r}}\times\delta\tilde{\boldsymbol{B}}^*\right)\cdot\boldsymbol{E}_T^0\,\mathrm{d}S, \tag{2.70}$$

$\forall\,\delta\boldsymbol{B}(\boldsymbol{r}) \in \tilde{V}_{0T}$.

Frequency-domain EMI with external boundary condition

Let $\omega > 0$ be the angular frequency, $\mu_0 > 0$ the magnetic permeability, $\rho(r,\vartheta,\varphi) \in L_\infty^+(G,\mathbb{R})$ the electric resistivity, and $\tilde{\boldsymbol{E}}^{\mathrm{imp}}(r,\vartheta,\varphi) \in L_2(G,\mathbb{C}^3)$ the imposed electric field. Let $\tilde{G}_{jm}^{(\mathrm{e})} \in \mathbb{C}$ be a set of external field coefficients for $j = 1,2,\ldots,\infty$ and $m = -j,\ldots,0,\ldots,+j$. Find $\tilde{\boldsymbol{B}}(\boldsymbol{r}) \in \tilde{V}_{0T}$ such that

$$\int_G \left(-\mathrm{i}\omega\mu_0\,\delta\tilde{\boldsymbol{B}}^*\cdot\boldsymbol{B} + \rho\,\mathrm{curl}\,\delta\tilde{\boldsymbol{B}}^*\cdot\mathrm{curl}\,\boldsymbol{B}\right)\mathrm{d}V = \int_G \mu_0\,\mathrm{curl}\,\delta\tilde{\boldsymbol{B}}^*\cdot\tilde{\boldsymbol{E}}^{\mathrm{imp}}\mathrm{d}V, \tag{2.71}$$

$\forall\,\delta\boldsymbol{B}(\boldsymbol{r}) \in \tilde{V}_0$, and

$$\int_{\partial G}\left[\frac{1}{j}\tilde{\boldsymbol{S}}_{jm}^{(+1)*} + \tilde{\boldsymbol{S}}_{jm}^{(-1)*}\right]\cdot\tilde{\boldsymbol{B}}\,\mathrm{d}S = -(2j+1)a^2\tilde{G}_{jm}^{(\mathrm{e})}, \tag{2.72}$$

$\forall\, j = 1,2,\ldots,\infty$ and $m = -j,\ldots,0,\ldots,+j$.

Table 2.1: Definitions of functional spaces used throughout the text.

$C^n(G;\mathbb{R}^k)$	real scalar (for $k=1$) and vector (for $k=3$) functions continuous up to the n-th derivative on the domain G
$L_2(G;\mathbb{R}^k)$	real scalar (for $k=1$) and vector (for $k=3$) functions, square-integrable in G. The spaces are equipped with scalar products $(f,g)_{L_2} = \int\limits_G f\, g \,\mathrm{d}V$ and $(\boldsymbol{f},\boldsymbol{g})_{L_2} = \int\limits_G \boldsymbol{f}\cdot\boldsymbol{g}\,\mathrm{d}V$ which generate the corresponding norms $\|f\|_{L_2} = (f,f)^{\frac{1}{2}}_{L_2}$ and $\|\boldsymbol{f}\|_{L_2} = (\boldsymbol{f},\boldsymbol{f})^{\frac{1}{2}}_{L_2}$
$L^+_\infty(G,\mathbb{R})$	real scalar positive functions bounded in G
H_{curl}	real vector functions $\boldsymbol{f} \in L_2(G;\mathbb{R}^3)$ such that $\mathrm{curl}\,\boldsymbol{f} \in L_2(G;\mathbb{R}^3)$. The space is equipped with a scalar product $(\boldsymbol{f},\boldsymbol{g})_{H_{\mathrm{curl}}} = \int\limits_G (\boldsymbol{f}\cdot\boldsymbol{g} + \mathrm{curl}\,\boldsymbol{f}\cdot\mathrm{curl}\,\boldsymbol{g})\,\mathrm{d}V$ and a corresponding norm $\|f\|_{H_{\mathrm{curl}}} = (f,f)^{\frac{1}{2}}_{H_{\mathrm{curl}}}$
$H_{\mathrm{curl},0}$	real vector functions $\boldsymbol{f} \in H_{\mathrm{curl}}$ such that $\boldsymbol{e}_{\mathrm{r}} \times \boldsymbol{f} = \boldsymbol{0}$ on ∂G
$H_{\mathrm{curl},0T}$	real vector functions $\boldsymbol{f} \in H_{\mathrm{curl}}$ such that $\boldsymbol{e}_{\mathrm{r}} \times \boldsymbol{f}_T = \boldsymbol{0}$ on ∂G, where $\boldsymbol{f}_T$ is the toroidal part of $\boldsymbol{f}$
H_{div}	real vector functions $\boldsymbol{f} \in L_2(G;\mathbb{R}^3)$ such that $\mathrm{div}\,\boldsymbol{f} \in L_2(G;\mathbb{R})$
H^0_{div}	real vector functions $\boldsymbol{f} \in H_{\mathrm{div}}$ such that $\mathrm{div}\,\boldsymbol{f} = 0$ in G
$H^{\frac{1}{2}}(\partial G;\mathbb{R}^3)$	real vector functions $\boldsymbol{f}(\boldsymbol{r}) \in L_2(\partial G;\mathbb{R}^3)$ such that $\lvert\boldsymbol{f}(\boldsymbol{r}) - \boldsymbol{f}(\boldsymbol{r}')\rvert / \lvert\boldsymbol{r}-\boldsymbol{r}'\rvert^2 \in L_2(\partial G \times \partial G;\mathbb{R})$
V	real vector functions $\boldsymbol{f} \in H_{\mathrm{curl}} \cap H^0_{\mathrm{div}}$
V_0	real vector functions from $\boldsymbol{f} \in H_{\mathrm{curl},0} \cap H^0_{\mathrm{div}}$
V_{0T}	real vector functions $\boldsymbol{f} \in H_{\mathrm{curl},0T} \cap H^0_{\mathrm{div}}$
$C^n\left(\overline{I};S\right)$	space of all mappings from the closed time interval $\overline{I} =< t_0, t_1 >$ to a functional space S, continuous up to the n-th derivative with respect to time. Various spaces of scalar or vector functions can take place of S, such as $C^n(G;\mathbb{R}^k)$, $L_2(G;\mathbb{R}^k)$, H_{curl}
$C^n(G;\mathbb{C}^k)$	complex scalar (for $k=1$) and vector (for $k=3$) functions continuous up to the n-th derivative on the domain G

$L_2(G;\mathbb{C}^k)$	complex scalar (for $k = 1$) and vector (for $k = 3$) functions, square-integrable in G. The spaces are equipped with scalar products $(f,g)_{L_2} = \int\limits_G f^* \, g \, \mathrm{d}V$ and $(\boldsymbol{f},\boldsymbol{g})_{L_2} = \int\limits_G \boldsymbol{f}^* \cdot \boldsymbol{g} \, \mathrm{d}V$ which generate the corresponding norms $\|f\|_{L_2} = (f,f)_{L_2}^{\frac{1}{2}}$ and $\|\boldsymbol{f}\|_{L_2} = (\boldsymbol{f},\boldsymbol{f})_{L_2}^{\frac{1}{2}}$
$\tilde{H}_{\mathrm{curl}}$	complex vector functions $\boldsymbol{f} \in L_2(G;\mathbb{C}^3)$ such that $\mathrm{curl}\,\boldsymbol{f} \in L_2(G;\mathbb{C}^3)$. The space is equipped with a scalar product $(\boldsymbol{f},\boldsymbol{g})_{H_{\mathrm{curl}}} = \int\limits_G (\boldsymbol{f}^* \cdot \boldsymbol{g} + \mathrm{curl}\,\boldsymbol{f}^* \cdot \mathrm{curl}\,\boldsymbol{g}) \, \mathrm{d}V$ and a corresponding norm $\|f\|_{H_{\mathrm{curl}}} = (f,f)_{H_{\mathrm{curl}}}^{\frac{1}{2}}$
$\tilde{H}_{\mathrm{curl},0}$	complex vector functions $\boldsymbol{f} \in \tilde{H}_{\mathrm{curl}}$ such that $\boldsymbol{e}_{\mathrm{r}} \times \boldsymbol{f} = \boldsymbol{0}$ on ∂G
$\tilde{H}_{\mathrm{curl},0T}$	complex vector functions $\boldsymbol{f} \in \tilde{H}_{\mathrm{curl}}$ such that $\boldsymbol{e}_{\mathrm{r}} \times \boldsymbol{f}_T = \boldsymbol{0}$ on ∂G, where $\boldsymbol{f}_T$ is the toroidal part of $\boldsymbol{f}$
$\tilde{H}_{\mathrm{div}}$	complex vector functions $\boldsymbol{f} \in L_2(G;\mathbb{C}^3)$ such that $\mathrm{div}\,\boldsymbol{f} \in L_2(G;\mathbb{C})$
$\tilde{H}^0_{\mathrm{div}}$	complex vector functions $\boldsymbol{f} \in H_{\mathrm{div}}$ such that $\mathrm{div}\,\boldsymbol{f} = 0$ in G
$\tilde{H}^{\frac{1}{2}}(\partial G;\mathbb{C}^3)$	complex vector functions $\boldsymbol{f}(\boldsymbol{r}) \in L_2(\partial G;\mathbb{C}^3)$ such that $\lvert\boldsymbol{f}(\boldsymbol{r}) - \boldsymbol{f}(\boldsymbol{r}')\rvert \,/\, \lvert\boldsymbol{r} - \boldsymbol{r}'\rvert^2 \in L_2(\partial G \times \partial G;\mathbb{R})$
$\tilde{V}$	complex vector functions $\boldsymbol{f} \in \tilde{H}_{\mathrm{curl}} \cap \tilde{H}^0_{\mathrm{div}}$
$\tilde{V}_0$	complex vector functions from $\boldsymbol{f} \in \tilde{H}_{\mathrm{curl},0} \cap \tilde{H}^0_{\mathrm{div}}$
$\tilde{V}_{0T}$	complex vector functions $\boldsymbol{f} \in \tilde{H}_{\mathrm{curl},0T} \cap \tilde{H}^0_{\mathrm{div}}$

The discretization of the weak formulations of the EMI equation is then based on the expansion of magnetic field into the real or complex vector spherical harmonic basis given by equation (2.56), which is complemented by the one-dimensional finite element parameterization,

$$B_{jm}^{(\lambda)}(r;t) = \sum_{k=0}^{k_{\max}+1} B_{jm}^{(\lambda,k)}(t)\psi_k(r), \tag{2.73}$$

where

$$\psi_k(r) = \begin{cases} \frac{r-r_{k-1}}{r_k-r_{k-1}} & \text{for } r_{k-1} \leqslant r \leqslant r_k, \\ \frac{r_{k+1}-r}{r_{k+1}-r_k} & \text{for } r_k \leqslant r \leqslant r_{k+1}, \\ 0 & \text{for } r < r_{k-1} \text{ or } r > r_{k+1}, \end{cases} \tag{2.74}$$

are the piecewise linear finite elements, and $(0 = r_1 < r_2 < \ldots r_{k_{\max}} < r_{k_{\max}+1} = a)$ is an arbitrary discretization of radial coordinate. It is further assumed that the electric resistivity ρ can be represented by piecewise constant functions along radial coordinate,

$$\rho(r, \vartheta, \varphi; t) = 1/\sigma(r, \vartheta, \varphi; t) = \sum_{k=1}^{k_{\max}} \rho_k(\vartheta, \varphi; t)\xi_k(r), \tag{2.75}$$

where

$$\xi_k(r) = \begin{cases} 1 & \text{for } r_k \leqslant r \leqslant r_{k+1}, \\ 0 & \text{for } r < r_{k-1} \text{ or } r > r_{k+1}. \end{cases} \tag{2.76}$$

The combined 3-D basis functions $\psi_k(r)\boldsymbol{S}_{jm}^{(\lambda)}(\Omega)$ for $k = 1, \ldots, k_{\max}+1$, $j = 1, \ldots, j_{\max}$, $m = -j, \ldots, j$, and $\lambda = -1, 0, 1$ define a discrete approximation of the space H_{curl} (or $\tilde{H}_{\text{curl}}$, using $\tilde{\boldsymbol{S}}_{jm}^{(\lambda)}(\Omega)$). The resolution is governed by two parameters, the number of radial layers $k_{\max}$, and the truncation degree of the spherical harmonic expansion $j_{\max}$. The discretizations of spaces $H_{\text{curl},0T}$ and $H_{\text{curl},0}$ are obtained by leaving out the basis functions $\psi_{k_{\max}+1}(r)\boldsymbol{S}_{jm}^{(0)}(\Omega)$ and $\psi_{k_{\max}+1}(r)\boldsymbol{S}_{jm}^{(0,+1)}(\Omega)$ from the parameterization, respectively. However, applying the divergence operator to the basis functions demonstrates that only the toroidal part, $\psi_k(r)\boldsymbol{S}_{jm}^{(0)}(\Omega)$ is divergence-free, i.e. from H_{div}^0. For the poloidal-scaloidal part, this condition can be enforced, and the scaloidal component suppressed in the weak formulations (2.64–2.66) by means of the Lagrange multipliers, adding a penalty term

$$\int_G \Lambda(\boldsymbol{r}; t)\text{div}\, \delta\boldsymbol{B}(\boldsymbol{r})\, \mathrm{d}V + \int_G \delta\Lambda(\boldsymbol{r})\text{div}\, \boldsymbol{B}(\boldsymbol{r}; t)\, \mathrm{d}V, \tag{2.77}$$

to the left-hand side, and finding $\Lambda(\boldsymbol{r}; t) \in C^0\left(\overline{I}; L_2(G, \mathbb{R})\right)$ together with $\boldsymbol{B}(\boldsymbol{r}; t)$ for all test functions $\delta\Lambda(\boldsymbol{r}) \in L_2(G, \mathbb{R})$. The solution and test function spaces V, V_0, and V_{0T} are then replaced respectively by H_{curl}, $H_{\text{curl},0}$, and $H_{\text{curl},0T}$. An analogous approach is used in the frequency domain (2.68–2.72) with $\tilde{\Lambda}(\boldsymbol{r}; t) \in L_2(G, \mathbb{C})$, $\delta\tilde{\Lambda}(\boldsymbol{r}) \in L_2(G, \mathbb{C})$, and complex

conjugation of the test functions in the penalty term. The Lagrange multipliers are expanded into scalar spherical harmonics, and piecewise constant radial functions as

$$\Lambda(\boldsymbol{r}) = \sum_{k=1}^{k_{\max}} \sum_{j=1}^{j_{\max}} \sum_{m=-j}^{j} \Lambda_{jm}^{k}\, \xi_k(r) Y_{jm}(\Omega). \tag{2.78}$$

Similarly, the imposed electric field $\boldsymbol{E}^{\mathrm{imp}}(\boldsymbol{r};t)$ is expanded as

$$\boldsymbol{E}^{\mathrm{imp}}(\boldsymbol{r};t) = \sum_{k=1}^{k_{\max}} \sum_{j=1}^{j_{\max}} \sum_{m=-j}^{j} \sum_{\lambda=-1}^{+1} E_{jm}^{(\mathrm{imp},\lambda,k)}(t)\, \xi_k(r) \boldsymbol{S}_{jm}^{(\lambda)}(\Omega). \tag{2.79}$$

The coefficients $B_{jm}^{(\lambda,k)}(t)$ and $\Lambda_{jm}^{k}(t)$ are then ordered into into a real vector $\mathbf{x}(t)$ with dimension $N = j_{\max}(j_{\max}+2)\,(4k_{\max}+3)$, as

$$\mathbf{x}(t) = \left\{ \left\langle \left[\left(B_{jm}^{(\lambda,k)}(t) \right)_{m=0,1,-1,\ldots}^{j,-j} \right]_{j=1}^{j_{\max}} \right\rangle_{\lambda=0,-1,+1}, \left[\left(\Lambda_{jm}^{k}(t) \right)_{m=0,1,-1,\ldots}^{j,-j} \right]_{j=1}^{j_{\max}} \right\}_{k=1}^{k_{\max}}, \left\langle \left[\left(B_{jm}^{(\lambda,k_{\max}+1)}(t) \right)_{m=0,1,-1,\ldots}^{j,-j} \right]_{j=1}^{j_{\max}} \right\rangle_{\lambda=0,-1,+1}. \tag{2.80}$$

We use such ordering in which the spherical harmonic order m represents the innermost index, advancing alternatively the cosine and sine-type terms. The blocks of coefficients describing the toroidal field ($\lambda = 0$) are followed by the blocks of poloidal field coefficients and the Lagrange multipliers. The outermost index k corresponds to the radial coordinate.

The Galerkin discretization of the problems (2.64–2.66) then has the form of a linear system of N ordinary differential equations,

$$\mathbf{A}(t) \cdot \mathbf{x}(t) + \mathbf{M} \cdot \frac{\partial \mathbf{x}(t)}{\partial t} = \mathbf{b}(t), \tag{2.81}$$

with an initial condition $\mathbf{x}(t_0)$.

Let us investigate the structure of the individual vectors and matrices. The matrix $\mathbf{M}$ consists of integrals of the products of basis functions, which simplify due to the orthogonality of spherical harmonics and limited support of the radial piecewise linear elements,

$$\mu_0 \int_G \left[\psi_k(r) \boldsymbol{S}_{jm}^{(\lambda)}(\Omega) \right] \cdot \left[\psi_{k'}(r) \boldsymbol{S}_{j'm'}^{(\lambda')}(\Omega) \right] \mathrm{d}V = \mu_0 \delta_{jj'} \delta_{mm'} \delta_{\lambda\lambda'} N_{j\lambda} I_{kk'}, \tag{2.82}$$

where

$$I_{kk'} = \begin{cases} \int\limits_{\min(r_k, r'_k)}^{\max(r_{k+1}, r_{k'+1}, r_{k_{\max}+1})} \psi_k(r)\psi_{k'}(r) r^2 \,\mathrm{d}r & \text{for } |k - k'| \leqslant 1, \\ 0 & \text{otherwise.} \end{cases} \tag{2.83}$$

Here, the non-dashed indices determine matrix rows, while the dashed indices correspond to matrix columns. There are no terms in rows and columns corresponding to the Lagrange multipliers, and their test functions. Hence, the $\mathbf{M}$ matrix follows a block-tridiagonal structure with individual blocks being diagonal matrices,

$$\mathbf{M} = \begin{pmatrix} \boxslash & \boxslash & & & & & \\ \boxslash & \boxslash & \boxslash & & & & \\ & \boxslash & \boxslash & \boxslash & & & \\ & & \ddots & \ddots & \ddots & & \\ & & & \boxslash & \boxslash & \boxslash & \\ & & & & \boxslash & \boxslash & \end{pmatrix}. \tag{2.84}$$

The elements of matrix $\mathbf{A}(t)$ involve the volume integrals

$$\int\limits_G \rho(\boldsymbol{r}; t) \operatorname{curl} \left[\psi_k(r) \boldsymbol{S}^{(\lambda)}_{jm}(\Omega)\right] \cdot \operatorname{curl} \left[\psi_{k'}(r) \boldsymbol{S}^{(\lambda')}_{j'm'}(\Omega)\right] \mathrm{d}V, \tag{2.85}$$

$$\int\limits_G \xi_k(r) Y_{jm}(\Omega) \operatorname{div} \left[\psi_{k'}(r) \boldsymbol{S}^{(\lambda')}_{j'm'}(\Omega)\right] \mathrm{d}V, \tag{2.86}$$

corresponding respectively to the terms stemming from the original weak formulations (2.64–2.66), and the addition of the divergence-free constraint (2.77). Again, the local support of the finite elements in radial coordinate implies the block-tridiagonal structure of the matrix. However, the detailed arrangement of individual blocks is more complicated. For 1-D layers, where resistivity is independent on lateral coordinates, $\rho_k(\vartheta, \varphi; t) = \rho_k(t)$, the EMI equation is decoupled in spherical harmonic degree and order. This yields a single diagonal term for the toroidal harmonics $\lambda = 0$, and two sub- and super-diagonal terms for the poloidal field $\lambda = \pm 1$ and the Lagrange multipliers. In the layers with laterally varying resistivity, the blocks are densely populated. An example below shows a typical arrangement used for a single 3-D layer above a 1-D model of mantle and core, where $\boxtimes$ and $\circledast$ denote respectively the sparse

and dense blocks,

$$\mathbf{A} = \begin{pmatrix} \boxtimes & \boxtimes & & & & & & \\ \boxtimes & \boxtimes & \boxtimes & & & & & \\ & \boxtimes & \boxtimes & \boxtimes & & & & \\ & & \ddots & \ddots & \ddots & & & \\ & & & \boxtimes & \boxtimes & \boxtimes & & \\ & & & & \boxtimes & * & * & \\ & & & & & * & * & \end{pmatrix}. \tag{2.87}$$

The right-hand side vector $\mathbf{b}(t)$ is assembled from the integrals of the type

$$\mu_0 \int_G \sum_{k'=1}^{k_{\max}} \sum_{j'=1}^{j_{\max}} \sum_{m'=-j'}^{j'} \sum_{\lambda'=-1}^{+1} E_{j'm'}^{(\mathrm{imp},\lambda,k')}(t)\,\mathrm{curl}\left[\psi_k(r)\boldsymbol{S}_{jm}^{(\lambda)}(\Omega)\right]\cdot\left[\xi_{k'}\boldsymbol{S}_{j'm'}^{(\lambda')}\right]\mathrm{d}V =$$

$$\mu_0 \int_G \sum_{k'=\max(1,k-1)}^{k} \sum_{\lambda'=-1}^{+1} E_{jm}^{(\mathrm{imp},\lambda',k')}(t)\,\mathrm{curl}\left[\psi_k(r)\boldsymbol{S}_{jm}^{(\lambda)}(\Omega)\right]\cdot\left[\xi_{k'}\boldsymbol{S}_{jm}^{(\lambda')}\right]\mathrm{d}V, \tag{2.88}$$

where the orthogonality of spherical harmonics and local support of the radial finite elements has been used again.

The boundary conditions are implemented in the structure of matrices $\mathbf{A}$, $\mathbf{M}$, and vector $\mathbf{b}$ as follows. In the case of the Dirichlet boundary condition, the horizontal test functions in the uppermost radial node, $\psi_{k_{\max}+1}(r)\boldsymbol{S}_{jm}^{(0)}(\Omega)$ and $\psi_{k_{\max}+1}(r)\boldsymbol{S}_{jm}^{(+1)}(\Omega)$, are not used (hence approximating the $H_{\mathrm{curl},0}$ space), the matrix $\mathbf{A}$ has 1 on the respective diagonals. The vector $\mathbf{b}$ has 0 and the value of $B_{jm}^{(+1)}(a;t)$ at the respective row positions, thus making sure that $\boldsymbol{B}-\boldsymbol{B}^0 \in H_{\mathrm{curl},0}$. In the case of mixed boundary condition, only the toroidal test function $\psi_{k_{\max}+1}(r)\boldsymbol{S}_{jm}^{(0)}(\Omega)$ is removed from the system, and the additional surface integral

$$\mu_0 \int_{\partial G} \boldsymbol{e}_{\mathrm{r}} \times \left[\psi_{k_{\max}+1}(a)\boldsymbol{S}_{jm}^{(1)}(\Omega)\right]\cdot\sum_{j'm'} E_{j'm'}^{(0)}(t)\boldsymbol{S}_{j'm'}^{(0)}(\Omega)\,\mathrm{d}S =$$

$$\mu_0 a^2 j(j+1)E_{jm}^{(0)}(t) \tag{2.89}$$

is added to the corresponding position in the $\mathbf{b}$ vector. Finally, the external boundary conditions are implemented in a similar way to the Dirichlet case, however the boundary condition

$$B_{jm}^{(-1,k_{\max}+1)}(t) + (j+1)B_{jm}^{(+1,k_{\max}+1)}(t) = -(2j+1)G_{jm}^{(\mathrm{e})}(t), \tag{2.90}$$

is directly implemented into the structure of matrix $\mathbf{A}$ and vector $\mathbf{b}$.

Let us note that in the case of Dirichlet and mixed boundary conditions matrices $\mathbf{A}$ and $\mathbf{M}$ are symmetric. For the external boundary condition, the symmetry of individual diagonal blocks of matrix $\mathbf{A}$, and the antisymmetry of the blocks above and below the diagonal is preserved with the exception of the last block-row and block-column corresponding to the boundary layer.

In the frequency-domain cases (2.68–2.72), the Galerkin method yields a system of complex linear equations

$$\left(\tilde{\mathbf{A}} - \mathrm{i}\omega\mu_0\tilde{\mathbf{M}}\right) \cdot \tilde{\mathbf{x}} = \tilde{\mathbf{b}} \tag{2.91}$$

with complex Hermitian matrices $\tilde{\mathbf{A}}$ (except for the external boundary condition) and $\tilde{\mathbf{M}}$, and complex vectors $\tilde{\mathbf{x}}$ and $\tilde{\mathbf{b}}$ assembled in a similar way as in the time-domain case.

2.4 Time discretization and linear problem solution

A back-of-the-envelope estimate of the time step necessary in the application of an explicit time-integration scheme to equation (2.81) yields

$$\Delta t < \mu_0 \min(\sigma) \min(\Delta r)^2 \approx 10^{-6}\,\mathrm{H/m}\, 10^{-4}\,\mathrm{S/m}\, \left(10^3\,\mathrm{m}\right)^2 = 10^{-4}\,\mathrm{s}, \tag{2.92}$$

which makes the explicit approach prohibitive for most applications. The semi-implicit scheme introduced by Velímský and Martinec (2005) uses splitting of the $\mathbf{A}$ matrix,

$$\mathbf{A} = \mathbf{A}_{1\mathrm{D}} + \mathbf{A}_{3\mathrm{D}}, \tag{2.93}$$

where the first matrix is assembled using a 1-D background conductivity model, and the second term is based on the lateral deviations from that model. The matrix $\mathbf{A}_{1\mathrm{D}}$ consists only of sparse blocks, which are further separated by spherical harmonic degree and order j, m (Martinec, 1998; Velímský and Martinec, 2005), and the factorization can be reduced to a series of tridiagonal and banded-matrix problems for the toroidal and poloidal components, respectively. Therefore, it was treated implicitly in the time-integration scheme, while the effect of lateral conductivity/resistivity variations through matrix $\mathbf{A}_{3\mathrm{D}}$ multiplication was carried explicitly from the previous time step. Hoewever, for strongly laterally heterogeneous models,

as demonstrated in the benchmarks by Kelbert et al. (2014), the accuracy of this approach was lacking.

The recent versions of the time-domain, spherical harmonic finite element solver use the Crank-Nicolson integration scheme. The time discretization of equation (2.81) is written as,

$$\frac{\mathbf{A}_{i+1}\cdot\mathbf{x}_{i+1}+\mathbf{A}_i\cdot\mathbf{x}_i}{2}+\mathbf{M}\cdot\frac{\mathbf{x}_{i+1}-\mathbf{x}_i}{\Delta t}=\frac{\mathbf{b}_{i+1}+\mathbf{b}_i}{2}, \tag{2.94}$$

and after rearranging,

$$(2\,\mathbf{M}+\Delta t\,\mathbf{A}_{i+1})\cdot\mathbf{x}_{i+1}=(2\,\mathbf{M}-\Delta t\,\mathbf{A}_i)\cdot\mathbf{x}_i+\Delta t\,(\mathbf{b}_{i+1}+\mathbf{b}_i)\,, \tag{2.95}$$

where $\mathbf{x}_i$, $\mathbf{b}_i$, and $\mathbf{A}_i$ are related to time levels $t_i = t_0 + i\,\Delta t$ with constant time step.

The choice of the optimal linear solver of system (2.94) or (2.95) depends on time and memory constraints, and suitability for parallelization. The individual dense blocks in the $\mathbf{A}_i$ matrix have dimension $D = 4\,j_{\max}\,(j_{\max}+2)$, and making use of the symmetry properties, the total memory needed to store them scales as $(K_{3\mathrm{D}}+1)\,D\,(3D+2)/2$, where $K_{3\mathrm{D}}$ is the number of layers with lateral conductivity variations. The memory requirements of the sparse blocks of $\mathbf{A}_i$ and $\mathbf{M}$ are negligible. If the available memory capacity is sufficient (e.g., for $j_{\max} = 80$, and $K_{3\mathrm{D}} = 10$, this represents about 85 GB in double precission arithmetics), and if the matrix $\mathbf{A}$ is invariable in time, a direct solver making effective use of the matrix structure can be employed. The Thomas algorithm (Press et al., 1992) designed for the solution of tridiagonal problems can be extended to the block-tridiagonal case. The forward sweep is carried out only once, and it requires the factorization of block submatrices, making use of the sparsity for 1-D layers as needed. The computing time therefore scales as $(K_{3\mathrm{D}}+1)\,D^3$, and, since the factorization is performed in place, no additional memory except for pivoting indices is needed. However, the factorization of individual blocks has to be carried out sequentially, row-by-row, and therefore the parallelization can be implemented only within the individual block calculations, typically using the shared-memory parallelized subroutines of the LAPACK library. The backward sweep then involves a series of $(K_{3\mathrm{D}}+1)$ solutions of block systems with pre-factorized matrices, which are carried out at each time step.

When the matrix $\mathbf{A}_i$ changes due to the temporal conductivity variations, or when the required resolution prevents the storage of the dense blocks, a matrix-free iterative solver must

be employed. In the recent implementation, the preconditioned BiCGStab(l) algorithm (Sleijpen and Fokkema, 1993) is used. It requires calculation of the product of matrix $\Delta t\mathbf{A}_i + 2\mathbf{M}$ with arbitrary vectors and also a fast inversion of the preconditioner. Looking back at the matrix elements (2.85), the product with an arbitrary vector can be effectively calculated by expressing the spherical harmonic sums on a discrete spatial grid, multiplying by resistivity values on the same grid, and then integrating back into the spherical harmonic domain. Both the forward and inverse spherical harmonic transforms are based on the FFT algorithm in longitude, and Gauss-Legendre quadrature is implemented in colatitude. Details of this technique are described by Martinec (1998) and Velímský and Martinec (2005). The matrix elements are not stored, although it is useful to pre-calculate the values of the associated Legendre polynomials and radial finite-element integrals to speed up the process. The calculation of one product of $\mathbf{A}_i$ with a vector scales in time as $(K_{\mathrm{3D}} + 1)\, j_{\max}^3 \log_2 j_{\max}$. Parallelization of the matrix-vector product subroutine across shared or distributed memory architecture can be used in the loop over the model layers. The preconditioner is then realized through the use of matrix $\mathbf{A}_{\mathrm{1D}}$, a simplified version of $\mathbf{A}$ assembled for a 1-D resistivity model.

The parallelization process can be taken one step further if the number of computational nodes available significantly exceeds the number of model layers. In that case, equations (2.94) for some finite range of time index i (ideally divisible by the number of nodes) are regarded as one combined linear system, solved by the BiCGStab(l) algorithm. Distributed memory systems set up with a linear communication topology are well suited for this task as each node needs to exchange information only with its left and right neighbors.

For the solution of the frequency-domain complex linear system (2.91), the iterative solver with matrix-free calculations of the matrix-vector product is a natural choice. The preconditioner is again based on the 1-D conductivity model. Table 2.2 summarizes the different versions of the forward solver in recent publications.

Table 2.2: Overview of the recent applications of the forward spherical-harmonic solver.

target	**domain**	**maximum resolution**		**solver**	**reference**
		$j_{\max}$	K_{3D}		
mantle	time	16	180	semi-implicit	Velímský et al. (2012)
mantle	time frequency	40	151	semi-implicit iterative	Kelbert et al. (2014)

mantle	time	5	15	direct	Velímský (2013)
mantle	time	20	70	direct	Maksimov and Velímský (2017)
M_2 ocean tides	frequency	480	102	iterative	Velímský et al. (2018)
ocean circulation	time	60	11	direct	Velímský et al. (2019)
ocean circulation	time/ stationary	80/ 480	5	direct iterative	Šachl et al. (2019)
ocean circulation	time	240	50	iterative	Schnepf et al. (2019)

3 Inverse modelling

3.1 Global EM induction inverse problem

The primary goal of the inverse EM induction modelling on the global scale is to recover the distribution of electric conductivity in the deep Earth interior from observations of the magnetic (and to a limited extent also electric) fields at the surface, or in the space. Consequently, the electric conductivity is then used to constrain the thermal, mineralogical, and chemical state of the Earth, jointly with other geophysical methods. The formulation of the inverse problem has several prerequisities (Tarantola, 2005). First, a parameter space (manifold) has to be established. Avoiding the peculiarities of the functional inverse problem, we will further consider a finite-dimensional manifold $\mathcal{M}$, which contains all admissible conductivity models under a selected discretization. Second, the information on measurements of observable variables and their errors has to be provided on the finite-dimensional manifold $\mathcal{D}$. Third, a forward problem relating the model parameters with the data has to be defined. A probabilistic description of these independent pieces of information then allows us to find a solution of the inverse problem by conjunction of the individual probabilities. This general approach is associated with the problem of sampling of probability density functions and is applicable when the dimension of the model manifold is small, and the solution of the forward problem can be obtained quickly. Both these conditions are satisfied for the global EM induction modelling with a 1-D spherically symmetric electric conductivity. In the case of more complex models, the deterministic approach is employed. It is based on a minimization of a misfit functional on $\mathcal{M}$ that measures the distance of data prediction from their observed values and combines them with additional regularization constraints on the model parameters. Effective calculations of the gradient of the misfit in the model space are provided by means of the adjoint

problem solution. The individual building blocks of our inversion scheme are described in the following section.

3.2 Model parameters

Since the electric conductivity and resistivity are complementary positive-valued parameters — Jeffreys' parameters in the terminology introduced by Tarantola (2005) — a natural choice is to discretize the (decimal) logarithm

$$\log \frac{\sigma(\boldsymbol{r})}{\sigma_0} = -\log \frac{\rho(\boldsymbol{r})}{\rho_0}, \tag{3.1}$$

where $\sigma_0 = 1/\rho_0$ are arbitrary background electric conductivity and resistivity values used here to preserve correct dimensionality. The time variations of electric conductivity are neglected here, as they are relevant only as seasonal changes in the oceans, and constrained by direct observations (Tyler et al., 2017).

In the case of 1-D conductivity models, a natural choice is to assign constant conductivities to individual layers. Recalling the definition of the piecewise constant functions $\xi_k(r)$ from equation (2.76), we can write

$$\log \frac{\sigma(r)}{\sigma_0} = \sum_{k=1}^{k_{\max}} \mathrm{m}_k \xi_k(r), \tag{3.2}$$

and arrange the parameters m_k into the vector

$$\mathbf{m} = (\mathrm{m}_k)_{k=1}^{k_{\max}}. \tag{3.3}$$

The radial discretization of the inverse problem does not have to coincide with the discretization of the forward problem, and our codebase indeed admits a single parameter m_k to span the conductivity across multiple layers of the forward solver. However, for the sake of simplicity, it will not be explicitly considered here.

When lateral conductivity variations are present, several choices are possible. One way, as used in Velímský (2013), among others, is to expand the conductivity logarithm into the spherical harmonic basis in each layer,

$$\log \frac{\sigma(\boldsymbol{r})}{\sigma_0} = \sum_{k=1}^{k_{\max}} \sum_{j=0}^{j^{\sigma}_{\max}} \sum_{m=-j}^{j} \mathrm{m}_{jm,k} Y_{jm}(\Omega) \xi_k(r). \tag{3.4}$$

The lateral resolution of the conductivity model is then governed by the truncation degree $j^{\sigma}_{\max}$ which should be chosen well below the truncation of the forward solver $j_{\max}$. The coefficients $\mathrm{m}_{jm,k}$ are then included into the model vector $\mathbf{m}$ with dimension $M = \dim \mathcal{M}$, in analogy with the assembly of vector $\mathbf{x}$ in equation (2.80).

A grid parameterization of conductivity is also possible, and it has been used by Maksimov and Velímský (2017) to demonstrate the calculation of scattered fields. In this case, piecewise-constant basis functions are used for lateral dimensions,

$$\log \frac{\sigma(\boldsymbol{r})}{\sigma_0} = \sum_{k=1}^{k_{\max}} \sum_{l=1}^{N_\vartheta} \sum_{m=1}^{N_\varphi} \mathrm{m}_{lm,k} \xi_l(\vartheta) \xi_m(\varphi) \xi_k(r), \tag{3.5}$$

with corresponding discretizations of colatitude and longitude intervals. Equations (3.2), (3.4), and (3.5) can be summarized as

$$\sigma = \sigma(\boldsymbol{r}; \mathbf{m}), \tag{3.6}$$

$$\rho = \rho(\boldsymbol{r}; \mathbf{m}). \tag{3.7}$$

The space of admissible conductivity models can be constrained by providing additional a-priori information independent of electromagnetic field measurements. Several regularization functionals are implemented in our codebase, constraining the L_2 norm of the first or second spatial derivatives in the logarithmic space,

$$R^2(\mathbf{m}) = \frac{1}{V} \int_G \left\{ \begin{array}{c} \left| \mathrm{grad} \left(\log \frac{\sigma(\boldsymbol{r};\mathbf{m})}{\sigma_0} \right) \right|^2 \\ \left| \Delta \left(\log \frac{\sigma(\boldsymbol{r};\mathbf{m})}{\sigma_0} \right) \right|^2 \\ \left| \mathrm{grad}_\Omega \left(\log \frac{\sigma(\boldsymbol{r};\mathbf{m})}{\sigma_0} \right) \right|^2 \\ \left| \Delta_\Omega \left(\log \frac{\sigma(\boldsymbol{r};\mathbf{m})}{\sigma_0} \right) \right|^2 \end{array} \right\} \mathrm{d}V. \tag{3.8}$$

In some cases, e.g. when an a-priori 1-D model is well constrained, it can be useful to constrain only the lateral conductivity variations using the angular parts of the gradient or Laplacian operators. Note that the derivatives $\mathrm{D}_{\mathbf{m}} R^2(\mathbf{m})$ in the model space, where

$$\mathrm{D}_{\mathbf{m}}(\bullet) = \left(\frac{\partial}{\partial \mathrm{m}_1}, \frac{\partial}{\partial \mathrm{m}_1}, \ldots, \frac{\partial}{\partial \mathrm{m}_M} \right)^T (\bullet)\,, \tag{3.9}$$

is the M-dimensional gradient operator, can be obtained analytically.

3.3 External and internal sources

The energy driving the EMI process in the Earth's interior can be provided both by external and internal sources, described respectively by the coefficients $G_{jm}^{(\mathrm{e})}(t)$ and $E_{jm}^{(\mathrm{imp},\lambda,k)}(t)$ in the spherical harmonic representation. Although the EMI problem is linear with respect to the source terms, they can be eliminated from the equations only in the simplest case (external loading by a dipole in frequency domain). This is in contrast with the magnetotelluric problem, where local responses are usually used with the assumption of planar source. In the global inverse problem formulation we are thus left with three choices.

First, we can carry out a multivariate analysis of data to obtain the global or local/global response functions, and use multiple runs for individual spatio-temporal modes in the forward modelling (Püthe and Kuvshinov, 2014; Püthe et al., 2015).

The second option is to provide the source terms by an initial data analysis or from other sources, and use them in the forward and inverse modelling as fixed, error-free parameters. This approach is usually taken for the internal excitation in the oceans, where we rely on the accuracy of the ocean flows obtained by data-assimilative methods, and the main magnetic field models (cf. Grayver et al., 2016, 2017; Velímský et al., 2018). However, it can be also applied to the external sources, as is the case of the original Swarm Level 2 time-domain processing chain with the 3-D inversion (Velímský, 2013) following an external/internal field separation (Sabaka et al., 2013).

Finally, the description of the source terms can be incorporated into the model space $\mathcal{M}$. The choice of source model parameters and their relation to the source coefficients $G_{jm}^{(\mathrm{e})}(t;\mathbf{m})$ can be arbitrary. As sketched in Velímský (2013) and later implemented into our codebase, the simplest implementation is offered by a 1:1 approach: all external field coefficient at all time levels are ordered and included in $\mathbf{m}$. Obviously, the increase of the model space dimension M is enormous and must be compensated in the data. Additional a-priori information can be used to reduce the dimensionality. For example, assuming the external field as a result of multiple circular current loops (Sun et al., 2015), only few parameters defining the position and orientation of such loops, and their respective current amplitudes are needed. Ideally, the $G_{jm}^{(\mathrm{e})}(t;\mathbf{m})$ mapping should be accompanied by fast calculations of the derivatives

$\mathrm{D}_{\mathbf{m}} G^{(\mathrm{e})}_{jm}(t;\mathbf{m})$.

3.4 Data and misfit

So far, our formulation of the inverse problem is limited to the observations of magnetic field at the Earth's surface or in the space. Extension to other observable parameters, such as submarine cable voltages, is possible, but will require substantial modifications of the definition of the misfit function and the formulation of the adjoint problem. There are several ways to define the misfit functional. Let us assume a finite number D of vector measurements of the magnetic field $\boldsymbol{B}^{\mathrm{obs}}(\boldsymbol{r}_i, t_i)$ at positions $\boldsymbol{r}_i$ and times t_i, arranged into a vector $\mathbf{d}^{\mathrm{obs}}$. Then we can define the data misfit as

$$\begin{aligned}
\chi^2(\mathbf{m}) =& \frac{1}{2}\left(\mathbf{d}-\mathbf{d}^{\mathrm{obs}}\right)^T \cdot \mathbf{C}_D^{-1} \cdot \left(\mathbf{d}-\mathbf{d}^{\mathrm{obs}}\right) \\
=& \frac{1}{2}\sum_{i=1}^{D}\sum_{j=1}^{D}\left[\boldsymbol{B}(\boldsymbol{r}_i,t_i;\mathbf{m})-\boldsymbol{B}^{\mathrm{obs}}(\boldsymbol{r}_i,t_i)\right]\cdot \mathbf{w}_{D,ij}\cdot\left[\boldsymbol{B}(\boldsymbol{r}_j,t_j;\mathbf{m})-\boldsymbol{B}^{\mathrm{obs}}(\boldsymbol{r}_j,t_j)\right] \\
=& \frac{1}{2}\int\limits_{\mathbb{R}^3}\int\limits_{\mathbb{R}^3}\int\limits_{t_0}^{t_1}\int\limits_{t_0}^{t_1}\left[\boldsymbol{B}(\boldsymbol{r},t;\mathbf{m})-\boldsymbol{B}^{\mathrm{obs}}(\boldsymbol{r},t)\right]\cdot \mathbf{W}_D(\boldsymbol{r},\boldsymbol{r}';t,t')\cdot \\
& \left[\boldsymbol{B}(\boldsymbol{r}',t';\mathbf{m})-\boldsymbol{B}^{\mathrm{obs}}(\boldsymbol{r}',t')\right]\mathrm{d}V\mathrm{d}V'\mathrm{d}t\mathrm{d}t', \qquad (3.10)
\end{aligned}$$

where $\mathbf{C}_D$ is the data covariance matrix, $\mathbf{w}_{D,ij}$ are the individual 3×3 blocks of its inverse, and

$$\mathbf{W}_D(\boldsymbol{r},\boldsymbol{r}';t,t') = \sum_{i=1}^{D}\sum_{j=1}^{D}\mathbf{w}_{D,ij}\delta(\boldsymbol{r}-\boldsymbol{r}_i)\delta(\boldsymbol{r}'-\boldsymbol{r}_j)\delta(t-t_i)\delta(t-t_j), \qquad (3.11)$$

allows the transition from the discrete observations to the formalism of continuous variables.

The misfit definition introduced above assumes that the uncertainty information contained in the covariance matrix is related to point observations. If such information is instead available in the spherical harmonic domain, following a previous spherical harmonic analysis, one

could define the misfit as

$$\chi^2(\mathbf{m}) = \sum_{j=1}^{j_{\max}} \sum_{m=-j}^{j} \sum_{j'=1}^{j_{\max}} \sum_{m'=-j'}^{j'} \frac{\sqrt{(2j+1)\,(2j'+1)}}{8\pi(t_1-t_0)} \int_{t_0}^{t_1} \begin{pmatrix} \sqrt{j}\left[G_{jm}^{(\mathrm{e})}(\mathbf{m},t) - G_{jm}^{(\mathrm{e,obs})}(t)\right] \\ \sqrt{j+1}\left[G_{jm}^{(\mathrm{i})}(\mathbf{m},t) - G_{jm}^{(\mathrm{i,obs})}(t)\right] \end{pmatrix}^T \cdot \mathbf{C}_{jmj'm'}^{-1}(t) \cdot \begin{pmatrix} \sqrt{j'}\left[G_{j'm'}^{(\mathrm{e})}(\mathbf{m},t) - G_{j'm'}^{(\mathrm{e,obs})}(t)\right] \\ \sqrt{j'+1}\left[G_{j'm'}^{(\mathrm{i})}(\mathbf{m},t) - G_{j'm'}^{(\mathrm{i,obs})}(t)\right] \end{pmatrix} \mathrm{d}t, \tag{3.12}$$

where $\mathbf{C}_{jmj'm'}(t)$ are the 2×2 blocks of the covariance matrix relating the external and internal field coefficients for each degree and order at the same time level. This approach was used in Velímský (2013) for the special case of diagonal covariance matrix. If the covariance matrices $\mathbf{C}_D$ and $\mathbf{C}_{jmj'm'}^{-1}(t)$ are both identity matrices scaled by the same constant variance, and all observations are taken at $r = a$, the definitions (3.10) and (3.12) are equivalent.

The evaluation of the misfit gradient is based on the adjoint approach with detailed description presented in Maksimov and Velímský (2017). The derivations presented there are limited to the misfit definition (3.12) for the spherical harmonic basis with a diagonal covariance matrix and fixed, error-free source, $G_{jm}^{(\mathrm{e})}(t) = G_{jm}^{(\mathrm{e,obs})}(t)$. Here, we introduce a more general formula with a full covariance matrix. Having obtained the complete solution of the forward problem for a given vector of model parameters $\mathbf{m}$, we first calculate the adjoint source coefficients in the adjoint time $\hat{t} = t_1 - t$ as

$$\hat{G}_{j'm'}^{(\mathrm{e})}(\hat{t}) = -\sum_{j=1}^{j_{\max}} \sum_{m=-j}^{j} \frac{\sqrt{2j+1}}{\sqrt{2j'+1}} \frac{1}{t_1-t_0} \int_{\max(t_0,t_1-\hat{t})}^{t_1} \begin{pmatrix} \sqrt{j}\left[G_{jm}^{(\mathrm{e})}(\mathbf{m},\tau) - G_{jm}^{(\mathrm{e,obs})}(\tau)\right] \\ \sqrt{j+1}\left[G_{jm}^{(\mathrm{i})}(\mathbf{m},\tau) - G_{jm}^{(\mathrm{i,obs})}(\tau)\right] \end{pmatrix}^T \cdot \mathbf{C}_{jmj'm'}^{-1}(t) \cdot \begin{pmatrix} 0 \\ \sqrt{j'+1} \end{pmatrix} \mathrm{d}\tau. \tag{3.13}$$

The adjoint source is then used to drive the solution $\hat{\boldsymbol{B}}(\boldsymbol{r};t)$ of the adjoint problem. It is identical to the forward problem with the external boundary condition (2.66) with time t replaced

by the adjoint time $\hat{t}$. The gradient misfit is then calculated as

$$\begin{aligned}\mathrm{D}_{\mathbf{m}}\chi^2(\mathbf{m}) =& \frac{1}{4\pi a^3\mu_0}\int_G\int_{t_0}^{t_1}\mathrm{D}_{\mathbf{m}}\rho(\mathbf{m};\boldsymbol{r})\,\mathrm{curl}\,\hat{\boldsymbol{B}}\cdot\mathrm{curl}\,\boldsymbol{B}\,\mathrm{d}V\mathrm{d}t \\ &+\sum_{jm}\sum_{j'm'}\frac{\sqrt{(2j+1)\,(2j'+1)}}{4\pi(t_1-t_0)}\int_{t_0}^{t_1}\begin{pmatrix}\sqrt{j}\left[G^{(\mathrm{e})}_{jm}(\mathbf{m},t)-G^{(\mathrm{e,obs})}_{jm}(t)\right]\\ \sqrt{j+1}\left[G^{(\mathrm{i})}_{jm}(\mathbf{m},t)-G^{(\mathrm{i,obs})}_{jm}(t)\right]\end{pmatrix}^T\cdot \\ &\mathbf{C}^{-1}_{jmj'm'}(t)\cdot\begin{pmatrix}\sqrt{j'}\mathrm{D}_{\mathbf{m}}G^{(\mathrm{e})}_{j'm'}(\mathbf{m};t)\\ 0\end{pmatrix}\mathrm{d}t. \end{aligned} \tag{3.14}$$

The first term in equation (3.14) depends on $\mathrm{D}_{\mathbf{m}}\rho(\mathbf{m};\boldsymbol{r})$, which are the derivatives of the electric resistivity with respect to the model vector $\mathbf{m}$. Therefore, it conveys the relative sensitivity of the misfit to the changes of the model parameters defining the resistivity. The second term in equation (3.14) includes the explicit derivations of the external field with respect to the model parameters, $\mathrm{D}_{\mathbf{m}}G^{(\mathrm{e})}_{jm}(\mathbf{m};t)$.

For the sake of completeness, the gradient formulas corresponding to the misfit (3.10) defined in the spatial domain are presented here. The adjoint source is obtained by integrating the formula

$$\begin{aligned}\frac{\partial\hat{G}^{(\mathrm{e})}_{jm}}{\partial\hat{t}}(\hat{t}) =& -\frac{4\pi}{2j+1}\sum_{i=1}^{D}\sum_{i'=1}^{D}\left[\boldsymbol{B}(\boldsymbol{r}_i,t_i;\mathbf{m})-\boldsymbol{B}^{\mathrm{obs}}(\boldsymbol{r}_i,t_i)\right]\cdot\mathbf{w}_{D,ii'}\cdot \\ &\left[(j+1)\boldsymbol{S}^{(-1)}_{jm}(\Omega_{i'})-\boldsymbol{S}^{(+1)}_{jm}(\Omega_{i'})\right]\left(\frac{a}{r_{i'}}\right)^{j+2}\delta(t-t_{i'}).\end{aligned} \tag{3.15}$$

Again, driving the forward problem by the adjoint source, $\hat{\boldsymbol{B}}(\boldsymbol{r};t)$ is calculated, and we obtain

$$\begin{aligned}\mathrm{D}_{\mathbf{m}}\chi^2(\mathbf{m}) =& \frac{1}{4\pi a^3\mu_0}\int_G\int_{t_0}^{t_1}\mathrm{D}_{\mathbf{m}}\rho(\mathbf{m};\boldsymbol{r})\,\mathrm{curl}\,\hat{\boldsymbol{B}}\cdot\mathrm{curl}\,\boldsymbol{B}\,\mathrm{d}V\mathrm{d}t \\ &-\sum_{jm}\int_0^{t_1}\left\{\frac{2j+1}{4\pi}\frac{\partial\hat{G}^{(\mathrm{i})}_{jm}}{\partial\hat{t}}-\sum_{i=1}^{D}\sum_{i'=1}^{D}\left[\boldsymbol{B}(\boldsymbol{r}_i,t_i;\mathbf{m})-\boldsymbol{B}^{\mathrm{obs}}(\boldsymbol{r}_i,t_i)\right]\cdot\mathbf{w}_{D,ii'}\cdot\right. \\ &\left.\left[j\boldsymbol{S}^{(-1)}_{jm}(\Omega_{i'})+\boldsymbol{S}^{(+1)}_{jm}(\Omega_{i'})\right]\left(\frac{r_{i'}}{a}\right)^{j-1}\delta(t-t_{i'})\right\}\mathrm{D}_{\mathbf{m}}G^{(\mathrm{e})}_{jm}(t_{i'})\mathrm{d}t.\end{aligned} \tag{3.16}$$

Again, the first term corresponds to the sensitivity to the resistivity variations, while the second term is related to the external field model. Similar derivations can be carried out in the frequency domain with time integration and time derivative replaced by the summation over discrete frequencies, and multiplication by $-\mathrm{i}\omega\mu_0$, respectively.

3.5 Solution of the inverse problem

With the solution of the forward problem at hand, and the ability to obtain the respective gradients of the data misfit and regularization functional, we proceed to a solution of the regularized inverse problem:

For a given regularization parameter $\lambda > 0$, find $\tilde{\mathbf{m}}(\lambda)$ that minimizes the functional

$$F(\mathbf{m}; \lambda) = \chi^2(\mathbf{m}) + \lambda\, R^2(\mathbf{m}) \tag{3.17}$$

on the manifold $\mathcal{M}$. From a set of parameters λ, select $\tilde{\lambda}$ such that the parametric curve $[\chi^2\left(\tilde{\mathbf{m}}(\lambda)\right), R^2\left(\tilde{\mathbf{m}}(\lambda)\right)]$ has the maximum inflection in $\tilde{\lambda}$. The corresponding $\tilde{\mathbf{m}}(\tilde{\lambda})$ is the solution of the inverse problem.

The selection of optimal regularization parameter $\tilde{\lambda}$ is called the L-curve analysis (Hansen, 1992), and it is carried out visually in practice. A series of minimizations is run for decreasing values of λ, using regular sampling in a logarithmic scale. The L-curve is plotted, a rough position of the maximum inflection point is estimated, then λ is finely resampled in its vicinity, and additional regularized models are obtained. A further refinement is possible, but seldom needed. While the runs for individual values of λ are independent, and thus offer an additional level of parallelization, the minimization process for each λ is accelerated by starting from the last model obtained for a larger regularization value. A leapfrogging strategy represents a good compromise, where multiple inversion chains with sequentially decreasing λ are run in parallel, providing a sufficient sampling of the L-curve.

The individual minimization problems are solved by the standard limited-memory Broyden-Fletcher-Goldfarb-Shanno (L-BFGS) algorithm (Liu and Nocedal, 1989). The approximation of the inverse Hessian is built up during the iteration processes. However, the entire matrix is not stored, but it is represented only by several vectors updated through recursive formulas from the values of $F(\mathbf{m}; \lambda)$ and $\mathrm{D}_{\mathbf{m}} F(\mathbf{m}; \lambda)$. The latter is obtained with the help of the adjoint field calculation described above.

4 Conclusions

4.1 Selected applications

The methods of forward and inverse modelling of the EMI problem introduced in the previous chapters, were used in several applications. A brief overview is presented here. Full-length papers are appended at the end of this Thesis.

The paper by Velímský et al. (2006) describes a first attempt to apply the time-domain inversion to low-orbit satellite data. A selection of 11 storm events observed by the CHAMP satellite data was processed and inverted in terms of 1-D conductivity profile. The unregularized inverse problem was solved by grid search on a space of three- or four-layered models. The position of the upper/lower mantle interface was also recovered by the inversion in the three-layer model. Using just short excerpts of data, the resolution of the inversion in the lower mantle was poor. A reasonable upper bound of electric conductivity was obtained for the upper mantle.

The next study based on the CHAMP satellite data (Velímský, 2010) has already used the regularized 1-D inversion by the L-BFGS method with adjoint misfit calculations. A grid search method was used to study the data sensitivity in the vicinity of the optimal model. Seven years of data were used to constrain the conductivity of the lowermost parts of the Earth's mantle, and a small increase of conductivity in the D" layer was observed.

Velímský and Finlay (2011) applied the time-domain EMI modelling to study the separation of external and internal field at annual and longer time scales. The presence of a highly conductive metallic core can introduce a significant shift in the induced field and should be taken into account when processing the storm indices, such as the Dst index.

Velímský et al. (2012) returned to the problem of the D" conductivity. Using 3-D for-

ward modelling based on conductivity models assembled from different structures provided by mantle convection modelling, we have demonstrated that the interconnection of a highly conductive material in D" in the equatorial direction is a necessary prerequisite to detect it by 1-D inversion driven by the ring current. Even large volumes of the conductor can remain invisible if they are separated by more insulating material.

The methodological description of the 3-D time-domain inversion chain, developed as a component of the Swarm Level 2 facility (Olsen et al., 2013) is presented by Velímský (2013). The method is successfully tested on a closed-loop simulation involving assembly of synthetic signals of various origins (core, ionosphere, magnetosphere, and induced) along Swarm satellite tracks, subsequent extraction of the magnetospheric inducing and induced fields, and 3-D inversion to recover the shape and conductivity of a large-scale heterogeneity in the mid-mantle.

The paper by Maksimov and Velímský (2017) provides the details of the mathematical formulation of the adjoint problem. It demonstrates its application to calculate the misfit gradient. Moreover, scattered forward and adjoint solutions are introduced to produce the matrix of second misfit derivatives — the Hessian in the space of model parameters.

The process of electromagnetic induction by ocean tides is studied in Velímský et al. (2018). The frequency-domain spherical harmonic formulation is used here in comparison with a solver based on the contracting integral equation approach. We demonstrate that the galvanic coupling between the ocean and the upper mantle, related to the toroidal magnetic field in the oceans, must be taken into account in order to accurately predict the signatures of M_2 tidal flow at satellite altitude.

The study by Velímský et al. (2019) is dedicated to the electromagnetic induction signatures of large-scale ocean flows driven by thermal and mechanical interactions with the Earth's atmosphere. We predict a large toroidal magnetic field generated by the Antarctic Circumpolar Current and study how it can influence the observable poloidal field.

4.2 Ongoing research and future outlook

The interpretation of Swarm satellite data in terms of mantle 3-D electric conductivity has been for a long time stalled by the problem of external/internal field separation in the process called *Comprehensive modelling* (Sabaka et al., 2013). Only the very recent models of external and internal field coefficients, obtained with careful selection of data especially in the polar areas, start to provide meaningful results.

Figure 4.1 shows the preliminary results of a 3-D inversion of the latest processing (version 0501) of the Swarm-derived time series of external and internal spherical harmonic coefficients, compared to two previous studies based on the inversion of ground observatory data (Semenov and Kuvshinov, 2012; Sun et al., 2015). The resolution of our model is limited by spherical harmonic expansion to degree 3 (in the log-space) in each layer. Some features of the conductivity models are consistent across the different approaches. For now, it is a matter

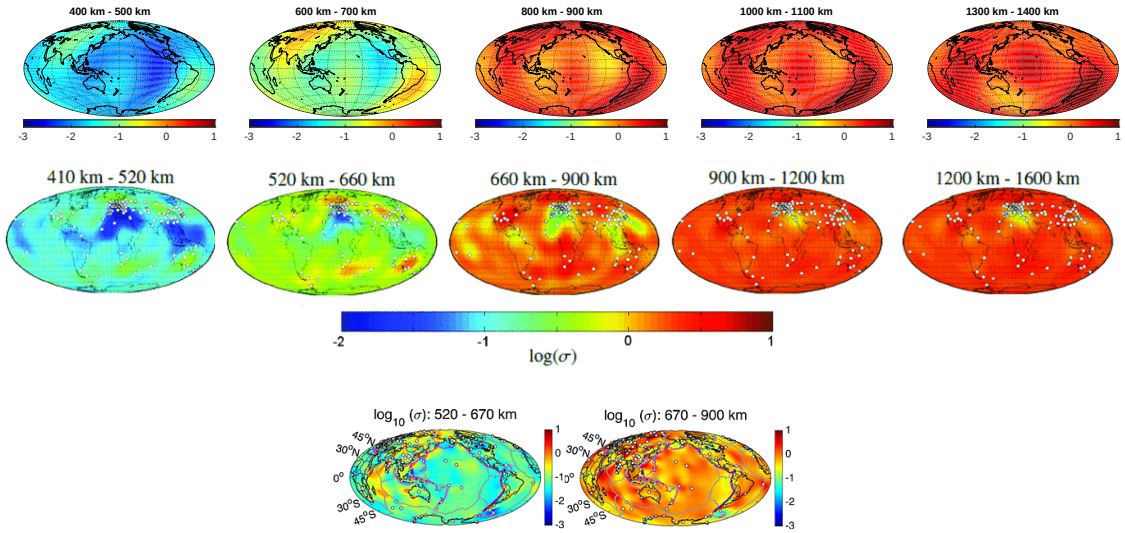

Figure 4.1: Top row: Selected cross-sections of a 3-D mantle conductivity obtained by Swarm satellite data inversion (Velímský & Knopp, unpublished). Middle row: Results of inversion of ground observatory data by Semenov and Kuvshinov (2012). Bottom row: Results of inversion of ground observatory data by Sun et al. (2015). Note that color scales differ between individual models.

of speculation, whether the resistive areas in the upper mantle coinciding with the *ring of fire* surrounding the Pacific Ocean are blurred signatures of the subducted plates.

Current efforts are concentrated on the co-estimation of the external field model together with the conductivity distribution, as suggested in Chapter 3. In particular, we aim to reduce the number of model parameters using the external field model consisting of multiple circular current loops.

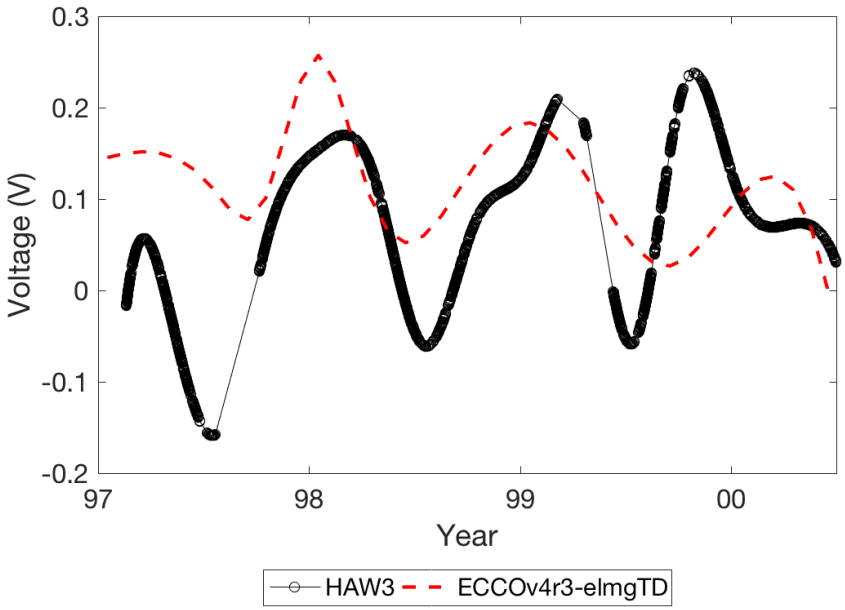

Figure 4.2: Comparison of observed and predicted voltages at submarine cable HAW3 (Makaha, Hawaii to San Luis Obispo, California). Modified from Schnepf et al. (2019).

Another recent application is the comparison of high-resolution predictions of the electric field generated by seasonal variations of ocean flows with measurements of electric voltages on submarine cables in the Pacific Ocean (Schnepf et al., 2019). Figure 4.2 shows one example of such a comparison. The submarine cable voltages observed during magnetic quite times were smoothed by cubic splines with 90 days knot separation. The high-resolution predictions of electric field at the seabottom were obtained by time-domain forward modelling of the EMI equation with seasonally variable conductivity (Tyler et al., 2017), and driven by the ocean flow model ECCO V4R3 (Forget et al., 2015). The electric field was then integrated along

the cable to provide the voltage difference between the endpoints. Although driven by the relatively weak East Pacific Gyre, there is significant correlation between the predicted signal and observed voltages. It remains an open question, whether such observations could be used for seasonal monitoring of large ocean currents, such as the Antarctic Circumpolar Current.

References

Arfken, G. B. and Weber, H. J. *Mathematical Methods for Physicists — International Edition*. Academic Press, San Diego, 6th edition edition, 2005.

Backus, G. Poloidal and toroidal fields in geomagnetic field modeling. *Reviews in Geophysics*, 24:75–109, 1986.

Berger, M. and Hornig, G. A generalized poloidal-toroidal decomposition and an absolute measure of helicity. *J. Phys. A: Math. Theor.*, 51:495501, 2018. 10.1088/1751-8121/aaea88.

Campbell, W. H. and Anderssen, R. S. Conductivity of the subcontinental upper mantle: an analysis using quiet-day geomagnetic record of North America. *J. Geomagn. Geoelectr.*, 35:367–382, 1983.

Campbell, W. H. and Schiffmacher, E. R. Upper mantle electrical conductivity for seven subcontinental regions of the Earth. *J. Geomagn. Geoelectr.*, 40:1387–1406, 1988.

Einšpigel, D. and Martinec, Z. Time-domain modelling of global ocean tides generated by the full lunisolar potential. *Ocean Dynamics*, 67:165–189, 2017. 10.1007/s10236-016-1016-1.

Everett, M. E. and Schultz, A. Geomagnetic induction in a heterogeneous sphere: Azimuthally symmetric test computations and the response of an undulating 660-km discontinuity. *J. Geophys. Res.*, 101:2765–2783, 1996.

Forget, G., Campin, J., Heimbach, P., Hill, C., Ponte, R., and Wunsch, C. ECCO version 4: An integrated framework for non-linear inverse modeling and global ocean state estimation. *Geoscientific Model Development*, 8:3071–3104, 2015. 10.5194/gmd-8-3071-2015.

Grayver, A. V., Schnepf, N. R., Kuvshinov, A. V., Sabaka, T. J., Manoj, C., and Olsen, N. Satellite tidal magnetic signals constrain oceanic lithosphere-asthenosphere boundary. *Science Advances*, 2:e1600798, 2016.

Grayver, A. V., Munch, F. D., Kuvshinov, A. V., Khan, A., Sabaka, T. J., and Tøffner-Clausen, L. Joint inversion of satellite-detected tidal and magnetospheric signals constrains electrical conductivity and water content of the upper mantle and transition zone. *Geophys. Res. Lett.*, 44:6074–6081, 2017.

Grayver, A. V., van Driel, M., and Kuvshinov, A. V. Three-dimensional magnetotelluric modelling in spherical Earth. *Geophys. J. Int.*, 217(1):532–557, 2019.

Hamano, Y. A new time-domain approach for the electromagnetic induction problem in a three-dimensional heterogeneous earth. *Geophys. J. Int.*, 150:753–769, 2002.

Hansen, P. Analysis of discrete ill-posed problems by means of the L-curve. *SIAM Review*, 34:561–580, 1992.

Irrgang, C., Saynisch, J., and Thomas, M. Impact of variable seawater conductivity on motional induction simulated with an ocean general circulation model. *Ocean Sci.*, 12(4): 129–136, 2016. 10.5194/os-12-129-2016.

Kelbert, A., Egbert, G., and Schultz, A. Non-linear conjugate gradient inversion for global EM induction: resolution studies. *Geophys. J. Int.*, 173:365–381, 2008.

Kelbert, A., Schultz, A., and Egbert, G. Global electromagnetic induction constraints on transition-zone water content variations. *Nature*, 460:1003–U85, 2009.

Kelbert, A., Kuvshinov, A., Velímský, J., Koyama, T., Ribaudo, J., Sun, J., Martinec, Z., and Weiss, C. J. Global 3-D electromagnetic forward modelling: a benchmark study. *Geophys. J. Int.*, 197:785–814, 2014.

Kuvshinov, A. Global 3-D EM studies of the solid Earth: Progress status. In Spichak, V. V., editor, *Electromagnetic Sounding of the Earth's Interior*, pages 1 – 21. Elsevier, Boston, second edition, 2015.

Kuvshinov, A. and Koch, S. 3-D EM inversion of ground based geomagnetic Sq data. Results from the analysis of Australian array (AWAGS) data. *Geophys. J. Int.*, 200(3):1284–1296, 2015.

Kuvshinov, A. and Semenov, A. Global 3-D imaging of mantle electrical conductivity based on inversion of observatory C-responses I. An approach and its verification. *Geophys. J. Int.*, 189:1335–1352, 2012.

Kuvshinov, A., Manoj, C., N., O., and T., S. On induction effects of geomagnetic daily variations from equatorial electrojet and solar quiet sources at low and middle latitudes. *J. Geophys. Res.*, 112:B10102, 2007. 10.1029/2007JB004955.

Kuvshinov, A. V. 3-D global induction in the oceans and solid earth: Recent progress in modeling magnetic and electric fields from sources of magnetospheric, ionospheric and oceanic origin. *Surveys in Geophysics*, 29(2):139–186, 2008. ISSN 1573-0956. 10.1007/s10712-008-9045-z.

Křížek, M. and Neittaanmäki, P. *Mathematical and Numerical Modelling in Electrical Engineering: Theory and Applications*. Kluwer Academic Publishers, Dordrecht, 1996. ISBN 0-7923-4249-6.

Liu, D. and Nocedal, J. On the limited memory method for large scale optimization. *Mathematical Programming B*, 45:503–528, 1989.

Maksimov, M. A. and Velímský, J. Fast calculations of the gradient and the Hessian in the time-domain global electromagnetic induction inverse problem. *Geophys. J. Int.*, 210:270–283, 2017.

Martinec, Z. Geomagnetic induction in multiple eccentrically nested spheres. *Geophys. J. Int.*, 132:96–110, 1998.

Martinec, Z. Spectral-finite element approach to three-dimensional electromagnetic induction in a spherical earth. *Geophys. J. Int.*, 136:229–250, 1999.

Martinec, Z., Velímský, J., Haagmans, R., and Šachl, L. A two-step along-track spectral analysis for estimating the magnetic signals of magnetospheric ring current from Swarm data. *Geophys. J. Int.*, 212:1201–1217, 2018.

Olsen, N., Friis-Christensen, E., Floberghagen, R., Alken, P., Beggan, C. D., Chulliat, A., Doornbos, E., da Encarnação, J. T., Hamilton, B., Hulot, G., van den IJssel, J., Kuvshinov, A., Lesur, V., Lühr, H., Macmillan, S., Maus, S., Noja, M., Olsen, P. E. H., Park, J., Plank, G., Püthe, C., Rauberg, J., Ritter, P., Rother, M., Sabaka, T. J., Schachtschneider, R., Sirol, O., Stolle, C., Thébault, E., Thomson, A. W. P., Tøffner-Clausen, L., Velímský, J., Vigneron, P., and Visser, P. N. The Swarm Satellite Constellation Application and Research Facility (SCARF) and Swarm data products. *Earth, Planets and Space*, 65(11):1189–1200, 2013.

Pankratov, O. and Kuvshinov, A. General formalism for the efficient calculation of the Hessian matrix of EM data misfit and Hessian-vector products based upon adjoint sources approach. *Geophys. J. Int.*, 200:1449–1465, 2015.

Pankratov, O. and Kuvshinov, A. Applied mathematics in EM studies with special emphasis on an uncertainty quantification and 3-D integral equation modelling. *Surv. Geophys.*, 37: 109–147, 2016.

Pankratov, O. V., Avdeev, D. B., and Kuvshinov, A. V. Scattering of electromagnetic field in inhomogeneous Earth: Forward problem solution. *Izv. Akad. Nauk SSSR Fiz. Zemli*, 3: 17–25, 1995.

Press, W. H., Teukolsky, S. A., Vetterling, W. T., and Flannery, B. P. *Numerical recipes in Fortran. The art of scientific computing*. Cambridge University Press, Cambridge, 1992.

Püthe, C. and Kuvshinov, A. Determination of the 3-D distribution of electrical conductivity in earth's mantle from swarm satellite data: Frequency domain approach based on inversion of induced coefficients. *Earth, Planets and Space*, 65:1247–1256, 2013.

Püthe, C. and Kuvshinov, A. Mapping 3-D mantle electrical conductivity from space: a new

3-D inversion scheme based on analysis of matrix Q-responses. *Geophys. J. Int.*, 197:768–784, 2014.

Püthe, C., Kuvshinov, A., and Olsen, N. Handling complex source structures in global EM induction studies: from C-responses to new arrays of transfer functions. *Geophysical Journal International*, 201(1):318–328, 2015. 10.1093/gji/ggv021.

Ribaudo, J. T., Constable, C. G., and Parker, R. L. Scripted finite element tools for global electromagnetic induction studies. *Geophys. J. Int.*, 188:435–446, 2012.

Sabaka, T. J., Tøffner-Clausen, L., and Olsen, N. Use of the Comprehensive Inversion method for Swarm satellite data analysis. *Earth, Planets and Space*, 65:1201–1222, 2013.

Schmucker, U. A spherical harmonic analysis of solar daily variations in the years 1964-65 – I. Methods. *Geophys. J. Int.*, 136(2):439–454, 1999a.

Schmucker, U. A spherical harmonic analysis of solar daily variations in the years 1964–1965: response estimates and source fields for global induction – II. Results. *Geophys. J. Int.*, 136 (2):455–476, 1999b.

Schnepf, N. R., Kuvshinov, A., and Sabaka, T. Can we probe the conductivity of the lithosphere and upper mantle using satellite tidal magnetic signals? *Geophys. Res. Lett.*, 42: 3233–3239, 2015.

Schnepf, N. R., Nair, M. C., Velímský, J., and Thomas, N. P. Can seafloor voltage cables be used to study large-scale transport? An investigation in the Pacific Ocean. *Earth, Planets and Space*, 2019. submitted.

Semenov, A. and Kuvshinov, A. Global 3-D imaging of mantle conductivity based on inversion of observatory C-responses–II. Data analysis and results. *Geophys. J. Int.*, 191(3): 965–992, 2012.

Seran, E., Godefroy, M., Pili, E., Michielsen, N., and Bondiguel, S. What we can learn from measurements of air electric conductivity in 222rn-rich atmosphere. *Earth and Space Science*, 4(2):91–106, 2017. 10.1002/2016EA000241.

Singer, B. Method for solution of Maxwell's equations in non-uniform media. *Geophys. J. Int.*, 120:590–598, 1995.

Sleijpen, G. L. G. and Fokkema, D. R. Bicgstab(ell) for linear equations involving unsymmetric matrices with complex spectrum. *Electronic Transactions on Numerical Analysis*, 1: 11–32, 1993.

Sun, J. and Egbert, G. D. A thin-sheet model for global electromagnetic induction. *Geophys. J. Int.*, 189(1):343–356, 04 2012. ISSN 0956-540X. 10.1111/j.1365-246X.2012.05383.x.

Sun, J., Kelbert, A., and Egbert, G. D. Ionospheric current source modeling and global geomagnetic induction using ground geomagnetic observatory data. *J. Geophys. Res. Solid Earth*, 120:6771–6796, 2015.

Šachl, L., Martinec, Z., Velímský, J., Irrgang, C., Petereit, J., Saynisch, J., Einšpigel, D., and Schnepf, N. R. Modelling of electromagnetic signatures of global ocean circulation: Physical approximations and numerical issues. *Earth, Planets and Space*, 71:58, 2019.

Tarantola, A. *Inverse problem theory and methods for model parameter estimation*. SIAM, Philadelphia, 2005.

Tyler, R. and Mysak, L. Electrodynamics in a rotating frame of reference with application to global ocean circulation. *Canadian Journal of Physics*, 73:393–402, 1995.

Tyler, R. H., Boyer, T. P., Minami, T., Zweng, M. M., and Reagan, J. R. Electrical conductivity of the global ocean. *Earth, Planets and Space*, 69:156, 2017.

Uyeshima, M. and Schultz, A. Geoelectromagnetic induction in a heterogeneous sphere: a new three-dimensional forward solver using a conservative staggered-grid finite difference method. *Geophys. J. Int.*, 140:636–650, 2000.

Varshalovich, D. A., Moskalev, A. N., and Khersonskii, V. K. *Quantum Theory of Angular Momentum*. World Scientific, Singapore, 1989.

Velímský, J. Determination of three-dimensional distribution of electrical conductivity in the Earth's mantle from swarm satellite data: Time-domain approach. *Earth, Planets and Space*, 65:1239–1246, 2013.

Velímský, J. and Martinec, Z. Time-domain, spherical harmonic-finite element approach to transient three-dimensional geomagnetic induction in a spherical heterogeneous Earth. *Geophys. J. Int.*, 160:81–101, 2005.

Velímský, J. Electrical conductivity in the lower mantle: Constraints from CHAMP satellite data by time-domain EM induction modelling. *Physics of the Earth and Planetary Interiors*, 180:111–117, 2010.

Velímský, J. and Finlay, C. Effect of a metallic core on transient geomagnetic induction. *Geochemistry, Geophysics, Geosystems*, 12:Q05011, 2011.

Velímský, J., Martinec, Z., , and Everett, M. Electrical conductivity in the Earth's mantle inferred from CHAMP satellite measurements — I. Data processing and 1-D inversion. *Geophys. J. Int.*, 166:529–542, 2006.

Velímský, J., Benešová, N., and Čížková, H. On the detectability of 3-D postperovskite distribution in D" by electromagnetic induction. *Physics of the Earth and Planetary Interiors*, 202-203:71–77, 2012.

Velímský, J., Grayver, A., Kuvshinov, A., and Šachl, L. On the modelling of M_2 tidal magnetic signatures: Effects of physical approximations and numerical resolution. *Earth, Planets and Space*, 70:192, 2018. 10.1186/s40623-018-0967-5.

Velímský, J., Šachl, L., and Martinec, Z. The global toroidal magnetic field generated in the Earth's oceans. *Earth and Planetatry Science Letters*, 509:47–54, 2019. 10.1016/j.epsl.2018.12.026.

Weiss, C. J. Triangulated finite difference methods for global-scale electromagnetic induction simulations of whole mantle electrical heterogeneity. *Geochem. Geophys. Geosyst.*, 11: 1525–2027, 2010.

Winch, D. E. Conductivity modelling of the Earth using solar and lunar daily magnetic variations. *J. Geophys.*, 55:228–231, 1984.

Wunsch, C. Low frequency variability in the sea. In Warren, B. and Wunsch, C., editors, *Evolution of physical oceanography*, pages 342–374. MIT Press, Cambridge, Mass., 1981.

Yoshimura, R. and Oshiman, N. Edge-based finite element approach to the simulation of geoelectromagnetic induction in a 3-D sphere. *Geophys. Res. Lett.*, 29(3):1039, 2002.

A Appendices

A.1 Velímský, J., Martinec, Z., and Everett, M.E., 2006. Electrical conductivity in the Earth's mantle inferred from CHAMP satellite measurements — I. Data processing and 1-D inversion. *Geophysical Journal International,* **166**, 529–542.

A.2 Velímský, J., 2010. Electrical conductivity in the lower mantle: Constraints from CHAMP satellite data by time-domain EM induction modelling. *Physics of the Earth and Planetary Interiors,* **180**, 111–117.

A.3 Velímský, J. and Finlay, C.C., 2011. Effect of a metallic core on transient geomagnetic induction. *Geochemistry, Geophysics, Geosystems,* **12**(5), Q05011.

A.4 Velímský, J., Benešová, N., and Čížková, H., 2012. On the detectability of 3-D post-perovskite distribution in D" by electromagnetic induction. *Physics of the Earth and Planetary Interiors,* **202–203**, 71–77.

A.5 Velímský, J., 2013. Determination of three-dimensional distribution of electrical conductivity in the Earth's mantle from Swarm satellite data: Time-domain approach. *Earth, Planets and Space,* **65**, 1239–1246.

A.6 Maksimov, M.A. and Velímský, J., 2017. Fast calculations of the gradient and the Hessian in the time-domain global electromagnetic induction inverse problem. *Geophysical Journal International,* **210**, 270–283.

A.7 Velímský, J., Grayver, A., Kuvshinov, A., and Šachl, L., 2018. On the modelling of M_2 tidal magnetic signatures: Effects of physical approximations and numerical resolution, *Earth, Planets and Space,* **70**, 192.

A.8 Velímský, J., Šachl L., and Martinec, Z., 2019. The Global Toroidal Magnetic Field Generated in the Earth's Oceans, *Earth and Planetary Science Letters,* **509**, 47–54.

A.1 Electrical conductivity in the Earth's mantle inferred from CHAMP satellite measurements — I. Data processing and 1-D inversion

Velímský, J., Martinec, Z., and Everett, M.E.

Published in *Geophysical Journal International* in 2006

Volume **166**, 529–542

doi: 10.1111/j.1365-246X.2006.03013.x

A.2 Electrical conductivity in the lower mantle: Constraints from CHAMP satellite data by time-domain EM induction modelling

Velímský, J.

Published in *Physics of the Earth and Planetary Interiors* in 2010

Volume **180**, 111–117

doi: 10.1016/j.pepi.2010.02.007

A.3 Effect of a metallic core on transient geomagnetic induction

Velímský, J. and Finlay, C.C.

Published in *Geochemistry, Geophysics, Geosystems* in 2011

Volume **12**, Number 5, Q05011

doi: 10.1029/2011GC003557

A.4 On the detectability of 3-D postperovskite distribution in D" by electromagnetic induction

Velímský, J., Benešová, N., and Čížková, H.

Published in *Physics of the Earth and Planetary Interiors* in 2012

Volume **202–203**, 71–77

doi: 10.1016/j.pepi.2012.02.012

A.5 Determination of three-dimensional distribution of electrical conductivity in the Earth's mantle from Swarm satellite data: Time-domain approach

Velímský, J.

Published in *Earth, Planets and Space* in 2013

Volume **65**, 1239–1246

doi: 10.5047/eps.2013.08.001

A.6 Fast calculations of the gradient and the Hessian in the time-domain global electromagnetic induction inverse problem

Maksimov, M.A. and Velímský, J.

Published in *Geophysical Journal International* in 2017

Volume **210**, 270–283

doi: 10.1093/gji/ggx167

A.7 On the modelling of M_2 tidal magnetic signatures: Effects of physical approximations and numerical resolution

Velímský, J., Grayver, A., Kuvshinov, A., and Šachl, L.

Published in *Earth, Planets and Space,* in 2018

Volume **70**, 192

doi: 10.1186/s40623-018-0967-5

A.8 The Global Toroidal Magnetic Field Generated in the Earth's Oceans

Velímský, J., Šachl, L., and Martinec, Z.

Published in *Earth and Planetatry Science Letters* in 2019

Volume **509**, 47–54

doi: 10.1016/j.epsl.2018.12.026